A progeria-associated BAF-1 mutation modulates gene expression and accelerates aging in *C. elegans*

Raquel Romero-Bueno[1] (ORCID ID 0000-0001-7454-2759), Adrián Fragoso-Luna[1], (ORCID ID 0000-0003-0325-7293), Cristina Ayuso[1] (ORCID ID 0000-0002-7179-4309), Nina Mellmann[1] (ORCID ID 0009-0000-6665-1285), Alan Kavsek[2] (ORCID ID 0009-0006-0310-6654), Christian G. Riedel[2,3] (ORCID ID 0000-0002-3689-8022), Jordan D. Ward[4] (ORCID ID 0000-0001-9870-8936) and Peter Askjaer[1] (ORCID ID 0000-0003-3192-4428)

AFFILIATIONS

[1] Andalusian Centre for Developmental Biology, Consejo Superior de Investigaciones Científicas (CSIC), Universidad Pablo de Olavide, Junta de Andalucía, Carretera de Utrera, km 1, 41013 Sevilla, Spain

[2] Department of Biosciences and Nutrition, Karolinska Institutet, Huddinge 14157, Sweden

[3] Faculty of Life Sciences: Food, Nutrition, and Health, Department of Nutritional Physiology, University of Bayreuth, 95326 Kulmbach, Germany

[4] Department of Molecular, Cell, and Developmental Biology, University of California-Santa Cruz, Santa Cruz, CA 95064, USA

Corresponding author: pask@upo.es

KEYWORDS

Aging, *BANF1*, Chromatin organization, Gene expression, NGPS, Nuclear lamina, Progeria, Stress resistance

ABSTRACT

Alterations in the nuclear envelope are linked to a variety of rare diseases termed laminopathies. These include both tissue specific and systemic diseases. A single amino acid substitution in human barrier to autointegration factor (BAF) at position 12 (A12T) causes Néstor-Guillermo Progeria Syndrome (NGPS). This premature ageing condition affects a variety of tissues, leading to growth retardation and severe skeletal defects, including scoliosis. Taking advantage of the conservation between human and *C. elegans* BAF proteins, we have modified the *baf-1* locus in *C. elegans* to mimic the human NGPS mutation (*baf-1(G12T)*). In this work, we characterized the phenotypes caused by the G12T mutation at molecular, cellular, and organismal scale. We found that the mutation induced multiple phenotypes related to fertility, lifespan, and stress resistance. Importantly, nuclear morphology deteriorated faster during aging in *baf-1(G12T)*, relative to wild-type animals, coinciding with an important hallmark of cells from progeria patients. Nuclear envelope accumulation of lamin and emerin was reduced whereas localization of BAF-1(G12T) was similar to wild-type BAF-1. We determined the chromatin binding profiles for wild-type and mutant BAF-1 and performed transcriptome analyses through tissue-specific DamID. Although the global profiles for wild-type and G12T BAF-1 resembled one another, we also identified many discrete regions with altered BAF-1(G12T) association. Most genes deregulated by the *baf-1(G12T)* mutation were characterized by a change in BAF-1 association, suggesting a direct relation between association of a gene to BAF-1 and its expression. We conclude that *C. elegans* is a relevant model to understand how a mutation in an essential

protein expressed throughout development triggers the appearance of symptoms in early childhood.

INTRODUCTION

The chromosomes in eukaryotic cells are physically enclosed by the nuclear envelope (NE), which protects them from mechanical stress and serves as an anchoring point for chromatin and associated factors (Manzo et al. 2022). The NE is composed of outer and inner nuclear membranes, the nuclear lamina, and nuclear pore complexes to facilitate nucleocytoplasmic transport. The nuclear lamina is a rigid meshwork that consists mainly of intermediate filament proteins called lamins as well as a variety of lamin-associated proteins, including integral inner nuclear membrane proteins. Nuclear organization is dynamic and changes during development and aging. Moreover, chromatin is differently organized in the diverse cell types within an organism (Ungricht and Kutay 2017). Furthermore, both environmental stress factors (such as temperature, pathogens, or nutrient availability) and internal factors (like cellular stress and mutations) can provoke changes in nuclear organization and gene expression. It is therefore not surprising that NE alterations are related to dramatic human conditions and attract intensive biomedical research efforts (Dobrzynska et al. 2016b; Shin and Worman 2022; Fragoso-Luna and Askjaer 2023).

Barrier to Autointegration Factor 1 (BAF/BANF1) is a small (89 amino acids) chromatin binding protein enriched at the NE and highly conserved across metazoans (Sears and Roux 2020). BAF acts as a homodimer that binds simultaneously to DNA, lamins, and inner nuclear membrane LEM (LAP2, emerin, MAN1) domain proteins, thus serving as an anchoring factor (Bradley et al. 2005; Samson et al. 2018). BAF was initially discovered as a factor required for retroviral infectivity (Lee and Craigie 1998). Its depletion is lethal during embryogenesis in *Caenorhabditis elegans* and *Drosophila melanogaster* (Zheng et al. 2000; Furukawa et al. 2003; Margalit et al. 2005) and decreases the survival of mouse and human embryonic stem cells (Cox et al. 2011). The localization of BAF at the NE is interdependent of its interaction partners, including lamins (Margalit et al. 2005; Lin et al. 2020), and LEM domain proteins, although BAF is also present in the nucleoplasm and the cytoplasm (Haraguchi et al. 2001; Margalit et al. 2007). BAF localisation during the cell cycle is controlled by phosphorylation: at the entry to mitosis vaccinia-related kinase 1 (VRK1) phospholylates BAF, which reduces its affinity for chromatin (Nichols et al. 2006; Marcelot et al. 2021). The protein phosphatase 2 (PP2A) complex dephosphorylates BAF at the end of mitosis, allowing reassociation of BAF to chromatin and NE components (Asencio et al. 2012). Interfering with BAF phosphorylation has severe consequences: when VRK1 is depleted from *C. elegans* embryos or human cells, BAF remains associated with chromosomes when cells enter mitosis, which leads to defects in chromosome segregation (Gorjanacz et al. 2007; Molitor and Traktman 2014). BAF is required for mitotic chromosome coherence and nuclear assembly towards the end of mitosis (Gorjanacz et al. 2007; Samwer et al. 2017). It localizes on the surface of the condensed chromosomes to maintain these tightly together, thereby ensuring the reassembly of a NE that encompasses all chromosomes in a single nucleus (Haraguchi et al. 2008; Samwer et al. 2017). More recently, BAF was implicated in the repair of NE ruptures (Halfmann et al. 2019). BAF localizes to the rupture site by binding to the leaking chromatin, and recruits LEM domain proteins to repair the NE and restore the permeability barrier (Young et al. 2020; Kono et al. 2022; Barger et al. 2023). Finally, BAF has also been involved in sensing mechanical stimuli to regulate cell cycle progression and DNA replication (Wang et al. 2018; Unnikannan et al. 2020).

About a decade ago, an identical homozygous amino acid substitution in human BAF (A12T) was identified in 2 patients (Néstor and Guillermo) suffering from premature aging symptoms, leading to the term Néstor-Guillermo progeria syndrome (NGPS) (Puente et al. 2011). NGPS

shares phenotypic similarities with Hutchinson-Gilford progeria syndrome (HGPS), which has been described in much greater detail and is most often caused by mutation in *LMNA* that encodes lamin A/C (Gonzalo et al. 2017). However, cardiovascular deficiencies and metabolic complications have not been described for NGPS patients and the manifestation of the condition occurs later, approximately 24 months after birth (Cabanillas et al. 2011). Similarly to HGPS, nuclear morphology is abnormal in NGPS fibroblast, and can be restored by expression of wild-type BAF (Puente et al. 2011; Janssen et al. 2022). It was proposed that the mutation destabilizes BAF (Puente et al. 2011), although this has been questioned by others (Paquet et al. 2014). The residue mutated in NGPS is situated close to the interface with lamin and the mutation was reported to reduce the affinity between the two proteins (Samson et al. 2018; Janssen et al. 2022). However, another study found that ectopically expressed BAF A12T localized correctly to the NE, and that the mutation modulated the affinity of BAF for DNA, thus possibly interfering with chromatin anchoring at the NE (Paquet et al. 2014). The A12T mutation was demonstrated to also affect NE rupture repair. Although mutant BAF A12T accumulated at rupture sites allowing repair, nuclei were observed to suffer repeated rupture more frequently than in control cells (Janssen et al. 2022). Despite the identification of several cellular defects in NGPS cells, it remains unclear what eventually leads to the patient phenotypes after seemingly normal foetal and postnatal development.

Almost all studies described above were performed with cultured cells. Although the use of patient-derived cell lines is essential to answer many of the open questions about NGPS, cell lines suffer limitations in terms of interplay between tissues and different organs (Yamamoto et al. 2024). To study the effect of the NGPS mutation in a whole-animal model, we introduced the equivalent mutation in the endogenous *baf-1* locus in *C. elegans*. We show that *baf-1(G12T)* mutants recapitulate several phenotypes typical of progerias, including shortened lifespan and accelerated deterioration of nuclear morphology. Moreover, the mutants have reduced fertility, increased sensitivity to irradiation and temperature stress but, surprisingly, are more tolerant to oxidative stress. We observed numerous changes in BAF-1's association with chromatin in hypodermal and intestinal cells, suggesting that the G12T mutation affects the affinity of BAF-1 for chromatin. By focusing on *baf-1's* role in chromatin organization, we identified genes that are both deregulated and differentially bound by BAF-1(G12T). Enriched gene classes include structural components of cuticle and ribosomes, suggesting specific functions of BAF in the regulation of gene expression. We conclude that *baf-1(G12T)* mutants serve as a relevant model to advance our understanding of BAF function and the mechanisms underlying NGPS.

RESULTS

The *baf-1(G12T)* mutation reduces brood size and lifespan

C. elegans and human BAF proteins share 74% amino acid sequence similarity (Margalit et al. 2005) and are predicted to adopt identical three-dimensional structures (**Supplementary Figure S1A**), making the worm a suitable model to study BAF mutations. To evaluate the effect of the NGPS mutation on *C. elegans* health span parameters, we modified the endogenous *baf-1* locus to encode a threonine residue at position 12 instead of the naturally occurring glycine.

We first measured fertility. At 20°C, *baf-1(G12T)* self-fertilizing hermaphrodites produced the same number of descendants as control worms (**Figure 1A**). In contrast, when worms were shifted to 25°C before reaching adulthood, their fertility was reduced by 66% (**FIG 1B**, **Supplementary Figure S1B**), whereas embryonic viability was unaffected (**Supplementary Figure S1C**). We noticed that *baf-1(G12T)* hermaphrodites deposited many unfertilized oocytes (UFOs) on the plates at 25°C (**Figure 1B**). *C. elegans* hermaphrodites usually lay a few UFOs when they run out of sperm (produced during the larval L4 stage) at the end of their reproductive cycle (Collins et al. 2008). However, *baf-1(G12T)* mutants laid UFOs throughout the fertile period, representing a 34% of the total lay versus only 6% in control animals (**Figure 1B**). We investigated

143 if the UFOs laid by *baf-1(G12T)* hermaphrodites at 25°C could be explained by a lack in sperm
144 production. However, we found sperm with the same frequency in the spermatheca of control
145 and *baf-1(G12T)* hermaphrodites on days 1 and 2 of adulthood (**Figure 1C, D**). On day 3, sperm
146 were still observed in approximately half of the control animals but in none of the *baf-1(G12T)*
147 mutants. These data indicate that although sperm were produced there might be defects in
148 function. To test this hypothesis, we mated *baf-1(G12T)* day 1 adult hermaphrodites with wild-
149 type males at 25°C for 7 hours. After mating we did not observe UFOs and the brood size was
150 comparable to self-fertilizing wild-type hermaphrodites (**Supplementary Figure S2A**). Mating
151 *baf-1(G12T)* hermaphrodites with *baf-1(G12T)* males also eliminated UFOs, but did not fully
152 restore the brood size, suggesting a sperm defect in *baf-1(G12T)* males (**Supplementary Figure**
153 **S2A**). To test this possibility, we incubated *baf-1(G12T)* males with *fog-2(q71)* feminized worms
154 that only produce oocytes and counted daily offspring. At 25°C, the *fog-2(q71)* allele prevents
155 spermatogenesis specifically in XX hermaphrodites whereas X0 males are unaffected (Schedl and
156 Kimble 1988). We observed a reduction in brood size of approximately one third when sperm
157 came from *baf-1(G12T)* males (**Supplementary Figure S2B, C**). Thus, we concluded that the *baf-*
158 *1(G12T)* mutation has a negative impact on spermatogenesis. The male/female ratio in the
159 progeny was ~1, suggesting that meiotic segregation of chromosomes was normal in *baf-*
160 *1(G12T)* males.

161 To gain insight into BAF-1 localization, we knocked GFP and mCherry (mCh) cassettes into the
162 endogenous *baf-1* and *baf-1(G12T)* loci to generate N-terminal fusions. We observed that BAF-
163 1 is present in mature sperm, both in males (**Supplementary Figure S3A**) and hermaphrodites
164 (**Supplementary Figure S3B**). In nematode sperm, chromosomes are surrounded by a poorly
165 defined halo that presumably lacks nuclear membranes (Wolf et al. 1978). GFP::BAF-1(G12T) is
166 also visible in sperm in hermaphrodites (**Supplementary Figure S3C**), indicating that BAF-1's
167 localization is not affected by the NPGS mimicking mutation. In contrast to BAF-1, we could not
168 detect endogenously tagged LMN-1 or EMR-1 in sperm of hermaphrodites (**Supplementary**
169 **Figure S3D**), nor LMN-1 in sperm in males (**Supplementary Figure S3E**). Moreover, the *baf-*
170 *1(G12T)* mutation did not induce localization of GFP::LMN-1 to sperm (**Supplementary Figure**
171 **S3F**).

172 We next evaluated if the NGPS mutation affected lifespan, as would be expected for a progeria
173 model. At 20°C, *baf-1(G12T)* hermaphrodites lived as long as control animals (**Supplementary**
174 **Figure S1D**). However, because lifespan correlates inversely with fertility (Arantes-Oliveira et al.
175 2002; Berman and Kenyon 2006), we speculated that the lower brood size in *baf-1(G12T)* at
176 restrictive temperature might counteract a potential shortening of their lifespan. To address
177 this, we first evaluated lifespan at 25°C in the presence and absence of the transcription factor
178 DAF-16, which is required to correlate fecundity with longevity (Hsin and Kenyon 1999). As
179 expected, depletion of DAF-16 reduced lifespan in wild-type hermaphrodites, as well as in *baf-*
180 *1(G12T)* ($p < 2e^{-16}$; **Figure 1E**). Importantly, the *baf-1(G12T)* mutation caused a reduction in
181 median lifespan at the restrictive temperature both in the presence (7% reduction; $p = 8e^{-13}$) and
182 absence (9% reduction; $p = 7e^{-10}$) of DAF-16 (**Figure 1E**). To completely eliminate the
183 confounding effect of the germ line on lifespan, we ablated the germ line by using the *glp-4(ts)*
184 mutation, which prevents germ cell proliferation at 25°C (Beanan and Strome 1992). We found
185 that median lifespan of sterile *glp-4(ts)* worms was reduced from 16 to 12 days (25% reduction;
186 $p < 2e^{-16}$) by the *baf-1(G12T)* allele (**Figure 1F**). These data indicate that the NGPS mutation
187 affects fecundity and lifespan in a temperature-dependent manner.

188 **Accelerated age-induced nuclear morphology deterioration in *baf-1(G12T)* mutants**

189 Alterations in NE morphology is associated with aging in several species, including *C. elegans*
190 (Haithcock et al. 2005; Perez-Jimenez et al. 2014) and also in human progeria syndromes
191 (Fragoso-Luna and Askjaer 2023). We therefore investigated morphology of nuclei in
192 hypodermal cells of wild-type and *baf-1(G12T)* animals at different ages. LMN-1 and EMR-1

193 endogenously tagged with GFP and mCherry (mCh), respectively, were used to visualize the NE
194 at day 1, 6 and 8 of adulthood in worms raised at 25°C. Nuclei were manually classified by single-
195 blind observer based on their morphology as previously described (Perez-Jimenez et al. 2014),
196 except that we introduced a fourth class to describe the most irregular nuclei (see Materials and
197 Methods). Thus, while class I nuclei have smooth, uniform NE signal, classes II-IV represent
198 progressive deterioration of nuclear morphology. At day 1, class I represented ~35% of nuclei
199 from wild-type worms and only ~20% of nuclei from *baf-1(G12T)* mutants when evaluated with
200 either GFP::LMN-1 or EMR-1::mCh (**Figure 2A-D**; $p < 0.03$; **Supplementary Table S1**). At day 6,
201 the number of class I nuclei in all strains was very reduced so we combined class I+II. Whereas
202 class I+II represented ~90% of nuclei from wild-type worms at day 1, at day 6, this fraction was
203 reduced to 27% according to GFP::LMN-1 (**Figure 2A, B**) and 42% according to EMR-1::mCh
204 (**Figure 2C, D**). The slightly more deteriorated morphology in animals expressing GFP::LMN-1
205 compared to EMR-1::mCh suggested that tagging of LMN-1 affects it function, as described
206 (Bone et al. 2016)(see also below). Regardless of the marker, significantly fewer class I and II
207 nuclei and more class III and IV nuclei were observed in *baf-1(G12T)* on day 6. Scoring EMR-
208 1::mCh, class I+II nuclei decreased from 42% in wild-type animals to 8% in *baf-1(G12T)* mutants
209 (**FIG 2D**; $p < 2.2e^{-16}$; **Supplementary Table S1**). Similarly, the frequency of class IV nuclei based
210 on GFP::LMN-1 localization increased from 10% in control animals to 23% in *baf-1(G12T)*
211 mutants (**Figure 2B**; $p = 0.0004$; **Supplementary Table S1**). We also evaluated nuclear
212 morphology after 8 days of adulthood at 25°C, which confirmed an increased deterioration in
213 *baf-1(G12T)* with both NE markers (**Supplementary Figure S4; Supplementary Table S1**). We
214 concluded that alterations in nuclear morphology are significantly accelerated in *baf-1(G12T)*
215 mutants at 25°C.

216 **Nuclear envelope accumulation of lamin and emerin is reduced by the *baf-1(G12T)* mutation**

217 The amino acid residue mutated in NGPS patients is positioned close to the interface between
218 BAF and lamin (Samson et al. 2018) and experimental evidence indicates that the interaction
219 between the two proteins is weakened by the mutation (Janssen et al. 2022). However, another
220 study suggested that the interaction was unaffected (Paquet et al. 2014). Because the
221 localization of BAF and lamins are interdependent (Margalit et al. 2005), impaired interaction
222 could drive reduced BAF-1 and lamin accumulation at the NE. To test the impact of *baf-1(G12T)*
223 on LMN-1, EMR-1, and BAF-1 localization *in vivo*, we quantified these factors at the NE of
224 hypodermal and intestinal cells. We observed significantly lower median GFP::LMN-1 signal at
225 the NE in *baf-1(G12T)* mutants in both tissues at 20°C and 25°C (**Figure 2E**; **Supplementary**
226 **Figure S5A-C**). In contrast, accumulation of EMR-1 at the NE was unaffected by the *baf-1(G12T)*
227 mutation in both tissues at 25°C and reduced in the hypodermis at 20°C (**Figure 2F**;
228 **Supplementary Figure S5D-F**). In human NGPS cells, emerin was observed to be delocalized to
229 the ER (Puente et al. 2011; Janssen et al. 2022), but we detected no increase in cytoplasmic EMR-
230 1::mCh signal in the mutant, indicating that this NGPS phenotype is not present in the *C. elegans*
231 model. In agreement with these microscopy data, analysis of whole-worm mRNA levels by
232 quantitative RT-PCR also revealed a significant reduction in *lmn-1* expression whereas *emr-1* was
233 unaffected (**Supplementary Figure S4E-F**).

234 Surprisingly, we found that the combination of *baf-1(G12T)* with the endogenously tagged
235 *gfp::lmn-1* allele *(yc32)* led to a fully penetrant maternal effect lethal (*mel*) phenotype:
236 homozygous *lmn-1(yc32[gfp::lmn-1]); baf-1(G12T)* embryos produced by hermaphrodites
237 heterozygous for the *yc32* allele developed all into adults that laid dead eggs at 20°C (**Figure 3A**).
238 We ruled out the possibility that the lethality was due to an unknown mutation in the genetic
239 background of the *yc32* allele by using a different endogenous *gfp::lmn-1* allele (*jf98*), which also
240 produced a 100% *mel* phenotype (**Supplementary Figure S6A**). In both cases, one copy of the
241 wildtype *lmn-1* allele was sufficient to sustain normal development.

242 To determine the subcellular defects that could explain the lethality of the allelic combination
243 *lmn-1(yc32[gfp::lmn-1]); baf-1(G12T)*, we recorded embryos by confocal 4D microscopy.
244 Chromosomes were visualized by co-expression of mCh::HIS-58, which revealed segregation
245 defects in early mitotic divisions and developmental arrest around 4-5h post-fertilization
246 (**Supplementary Figure S6B**). The early chromosome segregation defects prompted us to
247 investigate the embryos with higher temporal resolution. This uncovered abnormal pronuclear
248 appearance, incomplete sealing of the NE after mitosis and frequent chromosome bridges (6/10
249 embryos), which potentially is the primary cause to the observed lethality (**Figure 3B;**
250 **Supplementary Video S1**). Moreover, cell divisions were delayed (compare AB anaphase and P1
251 metaphase at 1049 sec in the control embryo versus 1149 sec in the *baf-1(G12T)* embryo). These
252 phenotypes are consistent with the effects of embryonic depletion of BAF-1 or LMN-1 (Liu et al.
253 2000; Margalit et al. 2005).

254 Next, we analyzed endogenously tagged *gfp::baf-1* and *gfp::baf-1(G12T)* nematodes. Strikingly,
255 whereas >99% of eggs laid by homozygous *gfp::baf-1* hermaphrodites developed and hatched,
256 all eggs laid by homozygous *gfp::baf-1(G12T)* hermaphrodites (derived from balanced,
257 heterozygous hermaphrodites) were inviable (**Figure 3C**). Similarly to the *lmn-1(yc32[gfp::lmn-*
258 *1]); baf-1(G12T)* embryos, the *gfp::baf-1(G12T)* embryos arrested before elongation
259 (**Supplementary Figure S7A**). Pronuclear appearance was severely affected and, in most
260 embryos, the two pronuclei failed to juxtapose prior to the first division (**Figure 3D;**
261 **Supplementary Video S2**; 4/7 embryos). Chromosome segregation and postmitotic nuclear
262 reformation were abnormal in all *gfp::baf-1(G12T)* embryos, presumably being causative for the
263 early developmental arrest. Cell division delays were also evident in all mutant embryos.

264 Finally, we compared GFP::BAF-1 and GFP::BAF-1(G12T) expression in adults and found that
265 both proteins accumulated at the nuclear periphery in all somatic cells and in the germ line
266 (**Supplementary Figure S7B**). Quantifying the intensity at the NE or in the nucleoplasm of
267 hypodermal cells did not demonstrate any difference between endogenously GFP-tagged wild-
268 type and mutant BAF-1 (**Figure 3E**). A small reduction in cytoplasmic signal was observed for
269 BAF-1(G12T), however, no difference was detected in the ratio between
270 nucleoplasmic/cytoplasmic signal (**Figure 3E**). Quantitative RT-PCR analysis of whole-worm RNA
271 samples also indicated that *baf-1* and *baf-1(G12T)* are expressed at identical levels
272 (**Supplementary Figure S4E-F**). Taken together, our results are compatible with a model in which
273 mutation of residue 12 of BAF reduces the affinity for lamin, leading to a mild reduction in the
274 accumulation of lamin as well as emerin at the NE. Moreover, the mutation sensitizes BAF so
275 tagging of either BAF-1(G12T) or lamin with GFP has detrimental effects on chromosome
276 segregation and NE assembly.

277 **The DNA binding profile of BAF-1 is modified by the G12T mutation**

278 BAF binds DNA *in vitro* without sequence specificity, and due to its location at the NE BAF has
279 been proposed to regulate chromatin organization (Zheng et al. 2000; Kind and van Steensel
280 2014). Moreover, human BAF A12T has been described to have altered DNA binding capacity
281 (Paquet et al. 2014), although others have disputed this claim (Marcelot et al. 2021). We decided
282 to test whether wild-type and mutant BAF-1 have different chromatin association profiles.
283 Because chromatin organization differs between tissues, subtle changes in chromatin
284 association of BAF-1(G12T) might not be detectable if averaging across multiple tissues. We
285 therefore performed tissue-specific DamID (DNA Adenine Methyltransferase Identification) by
286 expressing trace amounts of either Dam::BAF-1 or Dam::BAF-1(G12T) in two different tissues
287 using a FLP-FRT system (Munoz-Jimenez et al. 2017; Cabianca et al. 2019). We focused on the
288 hypodermis and the intestine because of skin atrophy and decreased subcutaneous fat in NGPS
289 patients (Cabanillas et al. 2011; Fisher et al. 2020).

290 DamID relies on the expression of the protein of interest fused to the DNA adenine
291 methyltransferase (Dam) of *Escherichia coli*. When the protein of interest binds chromatin, Dam
292 methylates GATC sites in close vicinity, which subsequently are identified through a series of
293 enzymatic reactions and deep sequencing (de la Cruz Ruiz et al. 2022). To normalize for
294 variations in chromatin accessibility, standard DamID protocols include a parallel sample based
295 on expression of Dam alone or Dam fused to a protein with no affinity for chromatin, such as
296 GFP. Thus, DamID can provide information about both chromatin accessibility and specific
297 binding profiles in the same experiment.

298 We first determined chromatin accessibility in L4 larvae from biological triplicates by binning
299 reads to 2kb bins (**Supplementary Figure S8A, B**). We identified 1924 bins with increased
300 accessibility in the hypodermis versus the intestine (3.8% of genome; FDR < 0.05) and 174 bins
301 with increased accessibility in the intestine (0.35% of genome). Examples of differential
302 accessibility include the genes *mua-6* and *dod-3*, which are expressed and more accessible in
303 hypodermis and intestine, respectively (**Figure 4A**). In contrast, we did not find evidence for
304 alterations in chromatin accessibility when comparing wild-type and *baf-1(G12T)* nematodes
305 and correlations were higher between the two genotypes within each replica than among
306 replicas of the same genotype (**Supplementary Figure S8A**). This suggests that BAF-1 does not
307 regulate compaction of interphase chromatin or that the mutation of residue 12 does not affect
308 this function.

309 We next calculated the log2 ratios between either Dam::BAF-1 or Dam::BAF-1(G12T) and
310 GFP::Dam to determine the binding profiles of BAF-1 and BAF-1(G12T). To visualize the global
311 distribution of the two proteins, the genome was binned into 100 kb windows. This revealed an
312 arm-center-arm pattern, where frequent association to BAF-1 or BAF-1(G12T) was detected in
313 the distal thirds of all autosomes but not in the central parts (**Supplementary Figure S9B**). The
314 pattern was highly similar between the two tissues, with few exceptions, such as the left arms
315 of chrIII and chrIV. Comparing the log2 values across all samples showed that the two tissues are
316 more dissimilar than BAF-1 and BAF-1(G12T) within each tissue (**Supplementary Figure S9A**).
317 The arm-center-arm pattern has been reported for other NE proteins, including LMN-1, EMR-1
318 and LEM-2 at different developmental stages (Ikegami et al. 2010; Towbin et al. 2012; Gonzalez-
319 Aguilera et al. 2014), as well as for the heterochromatin mark H3K9me (histone H3 methylated
320 on lysine 9) (Gerstein et al. 2010).

321 By increasing the resolution to 10 kb bins, we observed more continuous interaction of BAF-1
322 and BAF-1(G12T) on autosome arms in hypodermis versus intestine (**Figure 4B, C**). The G12T
323 mutation produced a small increase in association in chromosome centers specifically in the
324 hypodermis. We next identified bins significantly enriched for BAF-1 or BAF-1(G12T) association
325 and selected those for which the difference in log2 value between BAF-1 and BAF-1(G12T) was
326 >0.58 (equal to a fold change of 1.5). For BAF-1 in hypodermis, 410 bins on autosomes (5%)
327 fulfilled this criterium and the vast majority (87%) were located in arms (**Supplementary Table**
328 **S2**; $p < 2.2e^{-16}$). In contrast, for BAF-1(G12T) in hypodermis, enrichment was mostly observed in
329 chromosome centers (**Supplementary Table S2**; 478 enriched bins; $p = 5.0e^{-10}$). More bins were
330 differentially associated with BAF-1 or BAF-1(G12T) in intestine compared to hypodermis, but
331 they were more evenly distributed. We concluded that both BAF-1 and BAF-1(G12T) bound
332 predominantly to heterochromatin-enriched chromosome arms and that regions with subtle but
333 significant association to BAF-1(G12T) were also detected in chromosome centers in the
334 hypodermis.

335 **BAF-1(G12T) differential gene association**

336 Analysis at 2 kb bin and "gene level" (see Materials and Methods) enabled identification of genes
337 bound in the two tissues. Genome browser views illustrated again higher similarity between
338 BAF-1 and BAF-1(G12T) within tissues than either protein between tissues (**Supplementary**

339 **Figure S9C**). Nevertheless, many bins were predominantly bound by either wild-type or mutant
340 BAF-1 (**Figure 4D; Supplementary Figure S9C**). In the hypodermis, we identified 5,467 protein
341 coding and non-coding genes bound by BAF-1 and 6,376 genes bound by BAF-1(G12T)
342 (**Supplementary Table S3**). 4,541 genes (62%) associated with both proteins, whereas 2,761
343 genes (38%) are specific to either wild-type (926) or mutant (1,835) BAF-1 (**Figure 4E**). In the
344 intestine, 8,442 genes and 7,412 genes were bound by BAF-1 and BAF-1(G12T), respectively. Of
345 these, 5,410 genes (51%) were identified in both datasets, whereas 3,032 genes (29%)
346 associated specifically with BAF-1 and 2,078 genes (20%) specifically with BAF-1(G12T) (**Figure**
347 **4E**). Comparing all 4 datasets, 8,056 genes (62%) are present in at least two datasets whereas
348 4,839 genes (38%) are unique; 2,552 genes (20%) are bound by wild-type and mutant BAF-1 in
349 both tissues (**Supplementary Table S3**).

350 Analyzing the BAF-1 and BAF-1(G12T)-bound genes for tissue enrichment (Angeles-Albores et al.
351 2016) retrieved the categories *Nervous system*, *Epithelial system*, *Male*, and *Amphid sheath cell*
352 in both hypodermis and intestine and by both wild-type and mutant BAF-1 (**Figure 4F;**
353 **Supplementary Table S3**). In contrast, the categories *Reproductive system*, *Germ line*, and *Male*
354 *distal tip* were enriched for binding to wild-type BAF-1, but not BAF-1(G12T) in the hypodermis
355 (**Figure 4F**). For all these categories, except *Epithelial system*, genes are generally inactive in the
356 two tissues that we analyzed. This suggested that BAF-1 binding correlates inversely with gene
357 expression (see Discussion regarding the *Epithelial system*).

358 **Deregulation of ribosomal and cuticle genes in *baf-1(G12T)* mutants**

359 We next used tissue-specific RNA polymerase DamID (RAPID) (Gomez-Saldivar et al. 2020;
360 Fragoso-Luna et al. 2023) to identify genes expressed in hypodermis and intestine in wild-type
361 and *baf-1(G12T)* mutants. In wild-type animals, 1,960 genes were detected as expressed in
362 hypodermis and 1,585 genes in intestine (**Supplementary Table S4**). Of these, 491 genes were
363 shared between the two tissues. To explore if association to BAF-1 correlates with expression,
364 we calculated the median and average log2(Dam::BAF-1/GFP::Dam) values for genes expressed
365 in both tissues, in only one of them or in neither. In the hypodermis, we found that the log2
366 values were lowest for genes expressed in this tissue, whereas genes expressed in intestine had
367 intermediate values (**Figure 5A**). A similar picture emerged when analyzing genes expressed only
368 intestine (**Figure 5B**). These data suggest that expressed genes are generally depleted for
369 interaction with BAF-1.

370 By comparing hypodermal RAPID scores between wild-type and *baf-1(G12T)* we identified 36
371 genes that were reproducibly upregulated in the mutant and 26 genes that were downregulated
372 (**Figure 5C**; **Supplementary Table S4**). More genes were deregulated in the intestine with 76
373 genes being more expressed in *baf-1(G12T)* and 53 genes being repressed (**Figure 5D**;
374 **Supplementary Table S4**). Although only 0.9-2.5% of expressed genes in the two tissues were
375 deregulated, gene ontology (GO) analysis revealed a significant overrepresentation of several
376 GO terms. Genes related to histone acetylation, proton transport and ribosomes were
377 deregulated in both tissues, whereas other classes appeared only in hypodermis (e.g. cuticle
378 components) or intestine (**Figure 5E**).

379 Although we found that expressed genes are generally devoid of interaction with BAF-1, we
380 speculated that the deregulation of the genes identified in our RAPID experiments could be
381 related to altered BAF-1 binding. We plotted the DamID scores obtained with Dam::BAF-1(G12T)
382 versus Dam::BAF-1 for the deregulated genes, focusing initially on the intestine because of the
383 higher number of deregulated genes. The majority of deregulated genes had negative log2
384 scores, implying more frequent interaction with GFP::Dam than with either Dam::BAF-1 or BAF-
385 1(G12T). Surprisingly, both upregulated (**Figure 6A**) and downregulated (**Figure 6B**) genes had
386 higher log2 scores for BAF-1(G12T) compared to the wild-type protein. This result indicates that
387 deregulated genes are bound more often when BAF-1 it mutated. Two exceptions appeared

among the downregulated genes: F14E5.8 (an uncharacterized protein with no obvious ortholog in vertebrates) and *emr-1*, which both were bound by BAF-1 but not BAF-1(G12T) (**Figure 6B**). Whether BAF-1 is directly involved in transcriptional activation of these genes remains to be tested. As described above, the amount of endogenously tagged EMR-1::mCh at the NE of intestinal cells was normal in *baf-1(G12T)* mutants (**Supplementary Figure S5F**), suggesting a cellular capacity to buffer the downregulation of *emr-1* transcription (Vogel and Marcotte 2012). We also noted that among the 129 deregulated genes in the intestine, 13 encode ribosomal proteins (Q value = $2.4e^{-9}$). Strikingly, all 5 upregulated and 7/8 downregulated ribosomal genes had higher log2 scores with BAF-1(G12T) than with BAF-1 (**Figure 6A-C**; p = 0.0009). The genes that were deregulated in the hypodermis showed little difference in their interaction with the two versions of BAF-1 (**Supplementary Figure S10A, B**). However, genes encoding cuticle constituents were overrepresented (8/62 genes, Q value = $1.2e^{-6}$) and 7 of these showed decreased interaction with BAF-1(G12T) compared to BAF-1 (**Supplementary Figure S10C**; p = 0.03). Thus, although there is no uniform correlation between changes in association to BAF-1 and changes in gene expression, several gene classes appear to have specific behaviors.

BAF-1(G12T) induces alterations in stress resistance

Cells derived from HGPS patients suffer chronic oxidative stress and stimulation of antioxidant pathways can reverse cellular HGPS phenotypes (Kubben et al. 2016). Because of the similarities between NGPS and HGPS, we speculated that *baf-1(G12T)* mutants might be hypersensitive to oxidative stress. Surprisingly, we observed that *baf-1(G12T)* mutants survived longer than control animals upon exposure to tert-butyl hydroperoxide (**Figure 7A**; $p < 2e^{-16}$). Based on this result, we tested if the *baf-1(G12T)* mutants displayed changes in resistance to other systemic stressors. Gene ontology analysis suggested an enrichment in genes involved in *Response to X-ray baf-1(G12T)* mutants. We therefore exposed young adults to DNA damaging ultraviolet light and scored survival in the progeny. *baf-1(G12T)* mutants exhibited reduced survival in 7/8 samples (**Figure 7B**; p = 0.04), indicating that the ability to repair UV-induced DNA damage is compromised by the NGPS mutation. We next tested the response to acute heat stress, which provokes protein misfolding and aggregation and consequently activation of several response pathways, such as heat shock response, unfolded protein response and autophagy. When incubated at 35°C, the median survival of control hermaphrodites was 6 h versus 5 h for *baf-1(G12T)* mutants (**Figure 7C**; p = 0.00001). Thus, mutation of BAF-1 led to significantly reduced heat stress resistance and further studies should determine which response pathway(s) is impaired. We concluded that the NGPS mutation causes increased sensitivity to certain stress factors, but also that the mutation can protect against oxidative stress, which contrasts the situation in HGPS.

DISCUSSION

The need for a deeper understanding of healthy aging is becoming increasingly important, as the life expectancy of the world population has augmented in the last century. Studies on accelerating aging diseases have provided insight on different pathways that are altered during physiological aging, but specific mechanisms underlying these conditions have also emerged. The use of animal models is an instrumental source of knowledge due to the possibility of studying the effect of mutations and interventions at multiple scales. In this study, we established *C. elegans* as a model to study how a progeria-causing mutation in BAF affects nuclear organization, gene expression and physiology. Our work has provided insight not only to the differences in chromatin association between wild-type and mutant BAF-1 but also on tissue-specific interactions of BAF-1 with predominantly silent genes. The observation that nuclear morphology deteriorated faster in *baf-1(G12T)* mutants argues that *C. elegans* is a relevant model to investigate NGPS. Importantly, the differential sensitivities to irradiation,

437 temperature and oxidative stress suggest a complex organismal response to the G12T
438 substitution in BAF-1 and warrant further investigation. Recently, *Drosophila* was reported as
439 another invertebrate NGPS model, which revealed defects in centromere function and ovary
440 homeostasis (Duan et al. 2023). We anticipate that these two relatively simple animal models
441 will provide important platforms for both discovery and validation of potential targets and
442 treatments.

443 NGPS patient-derived fibroblasts exhibits partial delocalization of emerin from the NE to the
444 cytoplasm (Puente et al. 2011; Janssen et al. 2022). Although we observed a mild but significant
445 decrease in NE accumulation of EMR-1, we did not see an increase in cytoplasmic EMR-1 levels.
446 The behavior of emerin in the *Drosophila* NGPS model (Duan et al. 2023) was like the situation
447 in *C. elegans*, suggesting that emerin might be affected by the NGPS mutation in a species and/or
448 cell type-specific manner, for instance due to the presence or absence of other interaction
449 partners. NE accumulation of LMN-1 was also reduced in *baf-1(G12T)* mutants, which is
450 compatible with a model in which 1) lamin depends on BAF to localize at the NE (Margalit et al.
451 2005) and 2) the affinity of BAF for lamin is reduced by the NGPS mutation (Samson et al. 2018;
452 Janssen et al. 2022). We found that localization of BAF-1 itself was unaffected in the NE of *C.*
453 *elegans* somatic and germline tissues. This result contrasts with observations in flies, where the
454 NGPS mutation led to reduced NE accumulation (Duan et al. 2023). Different behaviors of BAF
455 A12T in human cells have been reported: ectopic expression showed in one study no difference
456 in the accumulation of wild-type and mutant BAF at the NE (Paquet et al. 2014), whereas another
457 study concluded that NE accumulation of BAF A12T was impaired (Puente et al. 2011). Finally,
458 using antibodies to compare endogenous BAF localization in control and NGPS fibroblasts found
459 a reduced nucleocytoplasmic ratio in the latter (Janssen et al. 2022).

460 Tagging BAF-1 and BAF-1(G12T) endogenously with GFP revealed a striking difference during
461 early development. Whereas tagging of wild-type BAF-1 had no obvious effect on fitness at any
462 stage of development, *gfp::baf-1(G12T)* embryos suffered severe nuclear appearance and
463 chromosome segregation defects already from the 1 cell-stage and all died before hatching. This
464 was in stark contrast with the ~100% viability of untagged *baf-1(G12T)* embryos. Surprisingly,
465 endogenous GFP tagging of LMN-1 also caused a fully penetrant embryonic lethal phenotype
466 when combined with the *baf-1(G12T)* allele. This lethality seemed specific to LMN-1 because
467 *emr-1::mCh; baf-1(G12T)* individuals developed normally. Moreover, timelapse recordings
468 unraveled similar defects in early *gfp::baf-1(G12T)* and *gfp::lmn-1; baf-1(G12T)* embryos. One
469 possible explanation is that GFP physically interferes with the interaction between BAF-1 and
470 LMN-1 and that this is only critical when BAF-1 carries the G12T mutation. Steric hindrance can
471 be envisioned both in the case of N-terminal tagging of BAF-1 because of proximity of BAF's N
472 terminus to the BAF·lamin interface, and in the case of N-terminal tagging of LMN-1 because
473 lamin dimers form head-to-tail polymers where the BAF-interacting globular domain of lamin
474 might be in proximity with the N terminus of the neighboring lamin molecule (Turgay et al. 2017;
475 Samson et al. 2018). In support of this hypothesis, animals with endogenously tagged LMN-1
476 and EMR-1 (*gfp::lmn-1; emr-1::mCh*) were fully viable, whereas we could not create a strain that
477 was homozygous for endogenous GFP::LMN-1 and mCh::BAF-1 (data not shown). We conclude
478 that insertion of fluorescent tags has a dramatic effect in *baf-1(G12T)* nematodes as well as in
479 flies (Duan et al. 2023). Although further studies are needed to determine the molecular
480 mechanism, we note that the high lethality of *gfp::lmn-1; baf-1(G12T)* embryos provides an ideal
481 sensitized genetic background to screen for suppressors (Breusegem et al. 2022).

482 Tissue-specific DamID unveiled that BAF-1 bound predominantly to the distal arms of
483 chromosomes, which are characterized by accumulation of repetitive elements and
484 heterochromatin marks, in particular methylation of histone H3 on lysine 9 (Gerstein et al. 2010;
485 Ahringer and Gasser 2018). In accordance with BAF-1's direct interactions with LMN-1, EMR-1
486 and LEM-2, DamID and chromatin immunoprecipitation profiles of these three proteins also

show enrichment in chromosome arms (Ikegami et al. 2010; Towbin et al. 2012; Gonzalez-Aguilera et al. 2014). Although the profiles of BAF-1 in hypodermis and intestine overlapped closely throughout most of the genome, we also detected regions larger than 100 kb that only interacted with BAF-1 in one of the tissues. At the level of individual genes, we found that expressed genes identified in our tissue-specific RAPID experiments were largely devoid of interaction with BAF-1. Although this was expected, based on the trend that genes positioned at the nuclear periphery are often transcriptionally silent (Ahringer and Gasser 2018; Manzo et al. 2022), our study represents the first mapping of BAF binding sites at gene resolution in any species. We observed an enrichment of BAF-1 at genes related to the nervous system and male-specific structures both in hypodermis and intestine where these genes are mostly silent. The appearance of the category *Epithelial system* as enriched for BAF-1 binding in hypodermis and intestine was surprising because we expected genes in this category to be expressed in these tissues. However, *Epithelial system* encompasses several thousand genes and inspection of the BAF-1-bound genes in this category revealed that <3% were detected as expressed in the hypodermis in our RAPID experiments or in another recent hypodermal transcriptomic dataset (Katsanos et al. 2021) (data not shown). We therefore concluded that BAF-1 binding in general correlates inversely with gene expression.

On a global scale, the chromatin association profile of BAF-1 and BAF-1(G12T) were highly similar, indicating that the NGPS mutation does not provoke chromosome repositioning. However, many changes were observed at the level of a few kb. In each of the two tissues, BAF-1 and BAF-1(G12T) bound 7,302-10,520 protein coding and non-coding genes (16-23% of all genes). More than half of the genes (51-62%) were shared between the wild-type and the mutant protein, whereas the number of uniquely bound genes ranged from 926 to 3,032 (13-29%). In the hypodermis, the different binding profiles manifested in several tissue enrichment analysis terms appearing only with wild-type BAF-1 (*Reproductive system*, *Germ line*, and *Male distal tip*). Despite the large number of genes that showed differences in association to BAF-1 versus BAF-1(G12T), relatively few genes were detected as deregulated. DamID-based methods, such as RAPID and TaDa, use RNA polymerase occupancy as a reliable proxy for gene expression (Southall et al. 2013; Gomez-Saldivar et al. 2020; Katsanos et al. 2021). However, subtle changes in transcription might not be detectable. Among the deregulated genes, several were related to metabolic processes (e.g. *Proton transport, ATP generation*, *Mitochondrial protein import*, etc.) and chromatin regulation (*Histone acetylation*). The most frequent deregulated genes were *Cuticle components* in the hypodermis and *Ribosome components* in both tissues. Seven of the eight deregulated cuticle genes in the hypodermis associated less frequently with BAF-1(G12T) than with BAF-1. For ribosomal genes the correlation was even more pronounced and in the opposite direction: 12 of the 13 deregulated ribosomal genes in the intestine associated less frequently with BAF-1(G12T) than with BAF-1. Surprisingly, in the intestine, both upregulated and downregulated genes bound more frequently to the mutant BAF-1 protein. The genes that changed both association with BAF-1 and expression level in the context of the G12T mutation might represent primary NGPS alterations. Importantly, translation levels and fidelity were observed to be altered in NGPS fibroblasts and depletion of ribosome components could improve several cellular parameters (Breusegem et al. 2022). At current, we can only speculate about how the NGPS mutation might affect gene expression. Proteomics analyses indicate that BAF interacts with several histones and transcription factors (Montes de Oca et al. 2009), and the differences between BAF-1 and BAF-1(G12T)'s chromatin binding profiles reported here might be accompanied by changes in the association of chromatin factors at the deregulated loci. A particularly interesting candidate is GCL-1/germ cell-less 1, a repressive factor involved in spermatogenesis (Holaska et al. 2003). Moreover, it is plausible that the diminished recruitment of LMN-1 to the NE in *baf-1(G12T)* mutants modifies its interaction with the genome and with chromatin factors.

537 Limited information is available on fertility in progeria patients (Donadille et al. 2013), but
538 mutations in components of the NE LINC (linker of nucleoskeleton and cytoskeleton) complex
539 cause infertility in several animal species (Link and Jantsch 2019). We observed a strong
540 reduction in brood size of *baf-1(G12T)* hermaphrodites at 25°C, which at least in part could be
541 ascribed to a diminished presence of sperm in the spermatheca. Sperm production in
542 hermaphrodites occurs during the L4 stage. The observation that the brood size phenotype
543 depended on incubation at 25°C during L4 stage or before points towards sperm-related defects.
544 Moreover, more than one third of the oocytes that passed through the spermatheca of *baf-*
545 *1(G12T)* hermaphrodites on day 1 of adulthood were not fertilized, despite sperm still being
546 present. This fertility defect was rescued by mating with wild-type males, suggesting that *baf-*
547 *1(G12T)* sperm were abnormal but oocytes unaffected. Mating feminized worms to *baf-1(G12T)*
548 males produced significantly fewer progeny compared to *fog-2* males, suggesting *baf-1(G12T)*
549 also causes defective male in sperm. Sperm, in contrast to oocytes, lack a typical nuclear
550 membrane. Instead, a halo on undefined composition encapsulates sperm DNA, RNA, and
551 centrioles (Wolf et al. 1978). In this study, we found that BAF-1 but neither LMN-1 nor EMR-1
552 was present in mature sperm in adults of both sexes. Moreover, the *baf-1(G12T)* mutation did
553 not alter this behavior. It is therefore possible that BAF-1 has a specific role in spermatogenesis
554 that is affected by the NGPS mutation, but further studies are required to explore this.

555 Stress resistance correlates positively with longevity, whereas alterations in stress response
556 pathways are intrinsically linked to diseases (Soo et al. 2023). In this context, we consider the
557 reduced resistance of *baf-1(G12T)* mutants to temperature stress and UV irradiation reported
558 in this study as a reflection of an overall impaired health span. We envision that they can be
559 explored as traits in future experiments designed to identify genes or compounds that improve
560 the health of *baf-1(G12T)* nematodes. However, the *baf-1(G12T)* mutation increased resistance
561 to oxidative stress, highlighting the complex interplay between different stress response
562 pathways and the need to evaluate potential interventions in multiple conditions to minimize
563 negative side effects. In this aspect, invertebrate models, like nematodes and flies, are very
564 attractive due to easy manipulation, low cost, and fast generation times (Yamamoto et al. 2024).
565 We note that the simplicity of invertebrates also implies certain limitations. For instance, while
566 both human and *C. elegans* genomes contain a single BAF gene, humans, but not *C. elegans*,
567 express multiple lamin isoforms in tissue-specific ratios that regulate chromatin organization
568 and nuclear mechanics (Swift et al. 2013). Thus, *C. elegans* is not suitable to explore potential
569 differences in how wild type and NGPS BAF interacts differently with the various lamin isoforms.

570 In conclusion, we have characterized the effect of introducing in *C. elegans* a mutation described
571 to cause NGPS in humans. Our results support the proposal that the NGPS mutation induces
572 changes in BAF's interaction with lamin and they are also consistent with the hypothesis that
573 the mutation alters BAF's affinity for chromatin. Importantly, *baf-1(G12T)* mutants reproduce
574 several progeria phenotypes, including reduced lifespan, accelerated nuclear deterioration,
575 lower fertility and altered stress resistance. We propose that these characteristics make *C.*
576 *elegans* a relevant model to study the molecular mechanisms of NGPS and to explore possible
577 interventions. Hopefully, combining the advantages of a simple *in vivo* model with those of
578 human cell and organoid cultures will lead to the discovery of efficient therapies.

579

580 **MATERIALS AND METHODS**

581 **Nematode strains and transgenesis**

582 Strains were maintained at 16°C or 20°C on Nematode Growth Medium (NGM) petri dishes
583 seeded with *Escherichia coli* OP50 using standard *C. elegans* methods (Stiernagle 2006). New
584 strains were generated by MosSCI (Frøkjær-Jensen et al. 2012; Dobrzynska et al. 2016a),
585 CRISPR/Cas9 (Arribere et al. 2014; Paix et al. 2015; Schwartz and Jorgensen 2016) and crossing

586 of existing strains. Descriptions and genotypes of all strains are listed in **Supplementary Table**
587 **S5**. The N2 strain was used as wild-type reference.

588 **Molecular cloning**

589 Plasmids pBN296 *hsp16.41p>mCh::his-58>dam::baf-1* and pBN298 *hsp16.41p>mCh::his-*
590 *58>dam::baf-1(G12T)* for DamID were constructed by amplifying *baf-1* and *baf-1(G12T)* with
591 primers B925 and B926 (see primer sequences in **Supplementary Table S6**) using genomic DNA
592 as template. The PCR product was digested with BglII and NheI and inserted into plasmid
593 pBN209 *hsp16.41p>mCh::his-58>dam::emr-1* (Cabianca et al. 2019) digested with the same
594 enzymes to replace *emr-1*.

595 Plasmid pBN566 *emr-1p::emr-1::mCh* with Frt sites in the first introns of *emr-1* and mCh was
596 made by insertion of a synthetic gBlock B840 into plasmid pBN20 (Morales-Martinez et al. 2015),
597 which contains 1568 bp upstream of the *emr-1* start codon, the *emr-1* CDS, mCh and 301 bp
598 downstream of the *emr-1* stop codon.

599 Plasmid pBN180 to insert and express sgRNAs from the promoter of R07E5.16
600 (WBGene00014484) was derived from pDD162 (Dickinson et al. 2013) by whole-plasmid PCR
601 with NEB Q5 polymerase and primers B633 and B634, deleting the Cas9 cassette. Plasmid
602 pBN180 was further modified by whole-plasmid PCR with primers B780 and B781 to generate
603 pBN215 that enables expression of sgRNA(E+F) (Ward 2015). Plasmids pBN207, pBN240 and
604 pBN485 to express sgRNAs corresponding to *dpy-10*, *emr-1* 3'-end and *emr-1* 5'-end,
605 respectively, were generated by whole-plasmid PCR with primer B635 and either primer B724
606 (*dpy-10*), B825 (*emr-1* 3'-end) or B838 (*emr-1* 5'-end) using either pBN180 (*dpy-10*) or pBN215
607 (*emr-1*) as PCR template. All DNA oligonucleotides were purchased from IDT.

608 **CRISPR/Cas9 genome editing**

609 Strain BN1007 *+/mT1 [umnIs34] II; baf-1(bq24[G>F>P::baf-1[G12T]])/mT1 [dpy-10(e128)] III* was
610 generated by microinjection of targeting plasmid pBN313 (Munoz-Jimenez et al. 2017) at 65
611 ng/µl into the gonads of BN868 *baf-1(bq19[G12T]) unc-119(ed3) III* young adult hermaphrodites
612 together with plasmids #1286 *eft-3p::Cas9* ((Friedland et al. 2013); 25 ng/µl), pBN1 *lmn-*
613 *1p::mCh::his-58* ((Rodenas et al. 2012); 10 ng/µl), pCFJ90 *myo-2p::mCh* ((Frøkjær-Jensen et al.
614 2008); 2.5 ng/µl) and pCFJ104 *myo-3p::mCh* ((Frøkjær-Jensen et al. 2008); 5 ng/µl). Successful
615 modification of the *baf-1(G12T)* locus was confirmed by detection of fluorescent fusion protein
616 in the NE, absence of ectopic mCherry expression from the co-injection markers and Sanger
617 sequencing. The *unc-119(+)* selection marker was next excised by microinjection with Cre
618 expression plasmid pMLS328 (Schwartz and Jorgensen 2016). Finally, uncoordinated
619 hermaphrodites were outcrossed to N2 males to remove the *unc-119(ed3)* allele and balanced
620 with mT1.

621 Strain BN1024 *emr-1(bq34[emr-1::mCh]) I* was generated by microinjection of repair template
622 plasmid pBN566 at 50 ng/µl into the gonads of N2 young adult hermaphrodites together with
623 plasmid #1286 *eft-3p::Cas9* (50 ng/µl), sgRNA plasmids (pBN207, pBN240 and pBN485; 25 ng/µl
624 each) and *dpy-10* single-stranded repair template B725 (500 nM). Successful modification of the
625 *emr-1(G12T)* locus was confirmed by detection of fluorescent fusion protein in the NE and
626 Sanger sequencing followed by outcrossing twice to N2.

627 Strain PMX375 was generated by CRISPR-mediated gene editing, introducing the mutation
628 c.34_35GG>AC into the endogenous *baf-1* locus, and then six times outcrossed to N2, to
629 eventually produce the strain BN808 *baf-1(bq19[G12T]) III*.

630 **Mos1-mediated single-copy integration**

631 Single-copy insertion of tissue-specific DamID constructs into the *ttTi5605* locus on chrII was
632 done by microinjection into the gonads of EG4322 young adult hermaphrodites. Plasmids

633 pBN296 and pBN298 carrying *unc-119(+)* as selection marker were injected at 50 ng/µl together
634 with pCFJ601 *eft-3p::Mos1* ((Frøkjær-Jensen et al. 2012), 50 ng/µl), pBN1 (10 ng/µl), pCFJ90 (2.5
635 ng/µl) and pCFJ104 (5 ng/µl). Integration of the constructs was confirmed by PCR and heat-
636 inducible expression of mCh::HIS-58.

637 **Lifespan assay**

638 Lifespan assays were performed as described (Haithcock *et al.* 2005). Animals were examined
639 every 1–3 days and transferred to fresh plates every day for the first 5 days and then every 5–7
640 days. For experiments involving RNA interference (RNAi), plates contained 1 mM IPTG and 25
641 µg/ml ampicillin were seeded with 100 µl of *E. coli* HT115 bacterial culture the previous day.
642 Control and *daf-16* RNAi proceeded from the Ahringer RNAi library (Kamath et al. 2003). Animals
643 that crawled off the plate or displayed extruded internal organs or internal hatching were
644 censored. Animals were considered dead when they failed to respond to gentle touch. Kaplan–
645 Meir curves were prepared and analyzed with R (R version 3.6.3) and R Studio (Version 1.1.463;
646 (Team 2020)). All experiments were performed at least in triplicate and combined, except the
647 results represented in Supplementary Figure S1D. Statistical analysis was performed by using
648 the R package survival that provides the chi-square statistic for a test of equality.

649 **Brood size assay**

650 Three to five L4 worms per strain and per replica were individually picked on NGM plates seeded
651 with *E. coli* OP50 and changed every 24 hours until eggs laying ceased. Parental animal that
652 crawled off the plate, dug into the agar, or suffered internal hatching precociously were
653 censored. Progeny was counted after 2 days of development. All experiments were performed
654 at least by triplicate. Statistical analysis was performed with R Studio using a two-tailed t-test.

655 **Nuclear morphology assay**

656 Three to five hermaphrodites per genotype grown at 25°C since L4 were observed at days 1, 6
657 and 8 after reaching L4 on each replica. Animals were anaesthetized with 10 mM levamisole and
658 mounted on thin 2 % agarose pads (de la Cruz Ruiz et al. 2022). A Nikon A1R microscope
659 equipped with a 60x objective was used to acquire confocal micrographs of hypodermal nuclei
660 every 1-2 µm from the surface of the worm to cover the entire depth of the hypodermis. Nuclear
661 morphology was classified into four groups without revealing the genotype of the specimens to
662 the researcher: class I) nuclei with uniform and smooth NE staining; class II) nuclei with
663 enhanced intranuclear staining of NE components and mildly lobulated nuclei; class III) nuclei
664 with highly irregular nuclear shape and accumulation of NE protein in bright foci concomitantly
665 with reduced peripheral signal; class IV) nuclei similar to class III but with protrusions of the NE
666 or ruptured NEs that release chromatin to the cytoplasm. All experiments were performed at
667 least by triplicate. Statistical analysis was performed by using Fisher's exact test in R Studio.

668 **Quantification of fluorescence intensity**

669 To quantify the fluorescence intensity of GFP::LMN-1, EMR-1::mCh, GFP::BAF-1 and GFP::BAF-
670 1(G12T), images of hypodermal nuclei were acquired as above and fluorescence intensity was
671 quantified with Fiji/ImageJ 2.1.0/1.53c (Schindelin et al. 2012) using the function Plot Profile of
672 a manually drawn, 5 pixel wide straight line across the entire nucleus. NE values were obtained
673 by averaging 3 consecutive values centered around the highest value on each side of the
674 nucleus. Nucleoplasm intensity values were determined by averaging consecutive 5 values from
675 the middle between the 2 NE maxima. Cytoplasm intensity values were determined by averaging
676 3 consecutive values 1 µm away from the NE on each side of the nucleus. Images of aged-
677 matched N2 worms were used as background. Statistical analysis was performed with R Studio
678 using a two-tailed t-test. Whereas quantification was performed on raw 12 bits images, identical
679 adjustment of brightness and contrast was applied to all comparable panels within each figure
680 panels.

681 **Time lapse recordings**

682 Embryos were obtained by cutting open gravid hermaphrodites using two 21-gauge needles,
683 mounted on a coverslip in 3 µl of M9 buffer. The coverslip was placed on a 2% agarose pad. For
684 high temporal resolution videos, 1 cell-stage embryos were recorded with a Yokogawa CSU-X1
685 spinning disc confocal scanning unit mounted on a Olympus IX-81 microscope equipped with
686 491 nm and 561 nm lasers and a 100x objective. Acquisition parameters were controlled by
687 MetaMorph software (v7.8.13.0). Z stack series consisting of 17 slices separated by 0.3 µm were
688 acquired every 12.5-20.4 sec followed by maximum projection for each time point. For
689 recordings of the entire embryonic development, coverslips were sealed with VALAP to avoid
690 desiccation and 5 confocal sections separated by 2 µm were acquired every 10 minutes on a
691 Nikon A1R microscope equipped with a 60x objective, Nikon Perfect Focusing System and 488
692 nm and 561 nm lasers. Single confocal sections were used for mounting figures. Room
693 temperature was 20-23°C. Images were processed using FIJI software, always applying identical
694 settings to control and mutant recordings.

695 **RNA purification**

696 Eggs were obtained by sodium hypochlorite treatment and incubated in M9 containing 0.01%
697 Tween-20 (M9-T) overnight at 20°C without food. For each strain, three 60 mm NGM plates with
698 a lawn of OP50 E. coli were seeded each with approximately 500 synchronized L1 larvae and
699 incubated at 20°C for 48 h until. L4 larvae were washed off the plates with M9-T, collected in 15
700 ml tubes and washed three times in M9-T. Finally, worms were pelleted in 1.5 ml tubes. The
701 supernatant was aspired to leave ~50 µl and 500 µl Trizol was added. Tubes were snap frozen in
702 liquid nitrogen and stored at -80°C.

703 Samples were lysed in 5 freeze/thaw cycles (1 min in liquid nitrogen; 3 min in 37°C shaker) and
704 left for 3 min at RT. Then, 100 µl chloroform was added, tubes were shaken vigorously for 15
705 seconds and left for 3 min at RT. After centrifugation at 12000 g, 4°C for 15 min, the aqueous
706 phases were transferred to new tubes containing 0.5 µl 20 mg/ml glycogen. RNA was
707 precipitated by adding 250 µl isopropanol and centrifugation at 12000 g, 4°C for 10 min.
708 Supernatants were removed and pellets were washed in 500 µl ethanol 75%. After
709 centrifugation and removal of the supernatants, the pellets were left to dry for 5 min and
710 resuspended in DEPC-treated water. Residual DNA was digested by treatment with DNase I
711 (NEB) in a total volume of 50 µl at 37°C for 10 min. DNase I was inactivated by addition of 0.5 µl
712 0.5 M EDTA. RNA was purified with NEB Monach spin columns, eluted in 20 µl DEPC-treated
713 water and evaluated on a Nanodrop.

714 **First-strand cDNA synthesis and quantitative PCR**

715 cDNA was prepared from 600 ng total RNA in a final volume of 40 µl using NZY First-Strand cDNA
716 Synthesis kit (NZYtech). Mixes were incubated at 25°C for 10 min and 55°C during 30 min.
717 Reactions were inactivated by heating for 5 min at 85°C. RNA was eliminated by adding 1 µl of
718 NZY RNase H during 30 min at 37°C. Quantitative PCRs were performed using NZYSupreme qPCR
719 Green Master Mix (2x) (see primer sequences in **Supplementary Table S6**). 2 µl of cDNA were
720 added in a final volume of 10 µl per reaction. Gene expression was evaluated in three
721 independent biological replicas, with three technical replicas each. The PCR program consisted
722 of 2 min at 95°C followed by 40 cycles of two steps, 5 sec at 95°C and 30 sec at 60°C. Melting
723 curves were determined by incubation at 65°C for 5 sec and at 95°C for 50 sec.

724 **Resistance to ultraviolet irradiation**

725 For every replica, 12-15 L4 hermaphrodites were isolated and grown at 20°C. Next day, five of
726 these worms were transferred to a new dish an irradiated in a Hoefer UVC 500 UV Crosslinker,
727 with a dose of 25 J/m2. In parallel, another five worms were isolated but were not exposed to
728 UV. Both, irradiated and non-irradiated worms were incubated for 2 hours at 20°C. Then, after

729 removing the adults, eggs were counted, and plates were incubated at 20°C. The day after,
730 larvae and non-hatched eggs were quantified. Statistical analysis was performed with R Studio
731 using a two-tailed paired t-test.

732 **Heat stress assay**

733 L4 worms were picked the day before the assay and maintained overnight at 20°C. The day of
734 the assay, thermotolerance resistance was evaluated by transferring 20 young adults to an NGM
735 plate without bacteria and incubated in a water bath at 35°C. Viability was scored every hour
736 after 2 hours and death was determined by the lack of movement and/or pharyngeal pumping
737 after gentle prodding. The experiment was performed in triplicate and the combined data were
738 analyzed as described for lifespan above.

739 **Oxidative stress assay**

740 The animals were synchronized as L1 larvae by egg-prepping with hypochlorite (Stiernagle 2006)
741 and hatching in M9. L1 larvae were then seeded onto 6 cm NGM plates containing 1 mM IPTG
742 and 50 µg/ml carbenicillin seeded with *E. coli* HT115 (transformed with the L4440 plasmid).
743 Animals were grown at 15°C until the late L4 stage, followed by the addition of 5-Fluoro-2'-
744 deoxyuridine (50 µM final concentration) and shifted to 20°C. At day 2 of the adulthood, animals
745 were washed off the plates with M9 and transferred to plates containing 6 mM tert-butyl
746 hydroperoxide (tBOOH). Seeding density was approximately 50 animals per plate. Plates were
747 then incubated at 20°C and the animals' survival was recorded and analyzed by a fully
748 automated lifespan machine as previously described (Stroustrup et al. 2013). For each condition,
749 a minimum of 150 worms distributed over at least 4 separate plates was scored. The combined
750 data were analyzed as described for lifespan above.

751 **Bacteria culture for DamID plates**

752 *E. coli* GM119 *dam-* was grown by pre-inoculating 1-2 colonies from a fresh LB/agar plate in
753 liquid LB without antibiotics. The pre-inoculum was grown overnight at 37°C before transferring
754 1 ml of culture to a suitable volume of LB (depending on the numbers of plates to be seeded,
755 i.e. for 10 plates with a diameter of 10 cm prepare at least 10 ml culture) and incubated for 6
756 hours at 37°C. Next, 700 µl of bacteria culture was added to each 10 cm NGM plate, spread and
757 incubated overnight at 37°C.

758 **Nematode culture for DamID**

759 Worms were grown asynchronically at 20°C on NGM plates seeded with *E. coli* GM119 for at
760 least two generations before egg-prepping with hypochlorite. Hatched L1s were counted the
761 day after and 1000 L1s were aliquoted onto 10 cm NGM plates seeded with *E. coli* GM119 as
762 described above. Worms were grown at 20°C for 48 h before collecting 4000 L4 stage nematodes
763 per strain and washed 8 times with 15 ml of M9 with 0.01% Tween-20. Worms were transferred
764 to 1.5 ml tubes with M9 with 0.01% Tween-20 using Pasteur pipettes followed by two additional
765 washes. Supernatants were aspirated and aliquots of 30 µl were snap frozen in liquid nitrogen
766 and maintained at -80°C until DNA extraction.

767 **DamID amplification, library preparation and sequencing**

768 To purify genomic DNA, samples were lysed in 5 freeze/thaw cycles (1min in liquid nitrogen;
769 3min in 37C shaker) and processed with DNeasy Blood and Tissue Kit (QIAGEN #69504). DamID
770 was performed on 200-400 ng genomic DNA (gDNA; 200 ng was used for RNA polymerase DamID
771 [RAPID]; 400 ng was used for BAF-1 and BAF-1(G12T) DamID) extracted from 4000 L4 animals
772 cultured and collected as indicated above. Two (RAPID) or three (BAF-1 and BAF-1(G12T) DamID)
773 replicates were performed as described (de la Cruz Ruiz et al. 2022). For RAPID, a pool of 3 AdR
774 primers (B1436 AdR4N, B1437 AdR5N, B1438 AdR6N) and 14 PCR cycles were used. For BAF-1
775 and BAF-1(G12T) DamID we used B916 AdR and 22 PCR cycles. Successful amplification of Dam-

776 methylated genomic DNA yielded a smear of ~400-~1500 bp fragments when analyzed on
777 Agilent Bioanalyzer.

778 Either 40 ng (RAPID) or 400 ng (BAF-1 and BAF-1(G12T) DamID) of PCR amplified fragments were
779 used for library preparation as described (de la Cruz Ruiz et al. 2022), using E7370 NEBNext®
780 Ultra™ DNA Library Prep Kit for Illumina. Library amplicons' size distribution was checked to be
781 maintained as for PCR fragments indicated above followed by pooling, repurification and
782 sequencing on a Illumina NextSeq500 platform at EMBL GeneCore.

783 **Bioinformatic analysis**

784 FASTQ files from the NextSeq500 platform were processed in R Studio using the pipelines
785 RDamIDSeq (https://github.com/damidseq/RDamIDSeq) and RGeneDamIDSeq
786 (https://github.com/damidseq/-RGeneDamIDSeq-) (Sharma et al. 2016) for mapping of reads to
787 bins of fixed size (e.g. 2 kb, 10 kb or 100 kb) and to genes, respectively. The pipelines include a
788 quality check where only reads that contain the DamID adapter ("CGCGGCCGAG") and map to
789 GATC sites in the *C. elegans* genome are retained for further analysis. The number of reads
790 fulfilling these criteria ranged from 0.5 to 27 million (see **Supplementary Table S7**). Both
791 pipelines also provide mapped read numbers per individual GATC fragment. For mapping to
792 genes, the script was modified to include 500 bp distal to transcriptional start and termination
793 sites. UCSC genome version ce11 (BSgenome.Celegans.UCSC.ce11) was used for alignment.

794 For BAF-1 and BAF-1(G12T) DamID the DESeq2 package (Love et al. 2014) was used to identify
795 bins with significantly more reads with either Dam::BAF-1 or Dam::BAF-1(G12T) compared to
796 GFP::Dam across the 3 replicas. A false discovery rate (FDR) of 0.05 was used as threshold. Next,
797 for each sample a pseudocount of 1 was added to each bin and the relative number of reads per
798 bin was calculated followed by averaging across the replicas. The ratio of Dam::BAF-1 or
799 Dam::BAF-1(G12T) to GFP::Dam was calculated for each bin and log2-transformed. Finally,
800 normalization was done by subtracting the genome-wide average log2 ratio from the log2 ratio
801 of each bin (Brueckner et al. 2020).

802 For RAPID, normalization of Dam::RPB-6 reads to GFP::Dam reads was performed using the
803 damidseq_pipeline package (https://owenjm.github.io/damidseq_pipeline/) (Marshall and
804 Brand 2015) on the bam files generated by the RDamIDSeq pipeline. Gene occupancy was
805 computed as log2(Dam::RPB-6/GFP::Dam) with polii.gene.call
806 (https://github.com/owenjm/polii.gene.call) using bedgraph output files from the
807 damidseq_pipeline and WBCel235 gene annotation. A FDR of 0.05 was used as threshold to call
808 transcribed genes.

809 For comparison of chromosome centers versus heterochromatin-rich distal arms, we used the
810 following border coordinates: ChrI 3745632 and 10809938, ChrII 4708341 and 11877168, ChrIII
811 3508994 and 9947268, ChrIV 7317812 and 12176625, ChrV 8125434 and 13849337, and ChrX
812 41919362 (Gonzalez-Aguilera et al. 2014). Pairwise Wilcoxon rank test values were calculated in
813 R.

814 Genome browser views and Venn diagrams were generated with the University of California
815 Santa Cruz Genomics Institute Genome Browser (http://genome.ucsc.edu; (Kent et al. 2002))
816 and jvenn (Web App) (Bardou et al. 2014), respectively. The WormBase Enrichment Suite
817 (http://www.wormbase.org/tools/enrichment/tea/tea.cgi; (Angeles-Albores et al. 2018)) was
818 used for tissue enrichment and gene ontology analysis.

819 Raw and processed DamID files are deposited at the NCBI Gene Expression Omnibus
820 (https://www.ncbi.nlm.nih.gov/geo/) with accession numbers GSE261819 (RAPID) and
821 GSE261820 (BAF-1 and BAF-1(G12T) DamID).

822

ACKNOWLEDGMENTS

We are grateful to Marta Rojas for assistance in genetic crosses, Laura Tomás from the CABD Proteomics and Biochemistry Facility for recombinant Cas9, Katherina García from the CABD Imaging Facility and Ildefonso Cases from the CABD Bioinformatics Facility for technical assistance, Vladimir Benes from EMBL GeneCore for advice on sequencing of DamID libraries and Delphine Larrieu for insightful comments. We also acknowledge the Caenorhabditis Genetics Center (CGC), which is funded by the National Institutes of Health (NIH) Office of Research Infrastructure Programs (P40 OD010440) and WormBase.

FUNDING

This project was funded by the Spanish Ministerio de Ciencia, Innovación y Universidades (MCIU), Agencia Estatal de Investigación, the European Union, the European Regional Development Fund (PID2019-105069GB-I00, CEX2020-001088-M, and PID2022-137162NB-I00; doi:10.13039/501100011033) and the Spanish Nacional Research Council, (2023AEP058). R.R.B. was supported by contract BES-2017-080216 from the Spanish MCIU and Scientific Exchange Grant 9276 from EMBO. J.D.W. was supported by the National Science Foundation (NSF) Division of Molecular and Cellular Biosciences (CAREER award 1942922). C.G.R. was supported by the Swedish Research Council (VR) (VR2023-04383), the Swedish Cancer Society (Cancerfonden) (23 2994 Pj), the Novo Nordisk Foundation (NNF22OC0078353). A.K. was supported by a Karolinska Institutet Doctoral Education Grant (KID).

FIGURE LEGENDS

Figure 1. Temperature sensitive brood size and lifespan reduction caused by *baf-1(G12T)* mutation. (A, B) Daily and total brood size was evaluated at 20°C (A) and at 25°C (B). For the wild-type (WT; blue columns) control, 14 and 41 adults were analyzed at 20°C and 25°C, respectively, whereas for *baf-1(G12T)* (red columns) the equivalent numbers were 11 and 42. Day 0 corresponds to the 24h interval from L4 to young adult and henceforth. Unfertilized oocytes (grey) were observed on *baf-1(G12T)* plates at 25°C already on day 0 and on control plates from day 2. Columns and error bars represent mean and standard deviation, respectively. (C, D) Presence of sperm in the spermatheca of wild-type and *baf-1(G12T)* hermaphrodites grown at 25°C and expressing mCh::HIS-58 was evaluated on days 1, 2 and 3. Representative images (C) with indication of spermatheca and sperm by dashed lines and arrows, respectively and combined results (D) from at least 7 animals at each time point and each strain. Scale bar represents 20 µM (E, F). Lifespan assay of wild-type and *baf-1(G12T)* hermaphrodites at 25°C fed with either control or *daf-16* RNAi bacteria (E) or germline-ablated *glp-4(ts)* mutants combined with either wild-type *baf-1* or *baf-1(G12T)* (F). Data combined from 3 (E) or 4 (F) independent experiments; the number of animals is indicated in brackets. P values from two-sided t-tests (A, B; asterisks and triangles refer to fertilized embryos and unfertilized oocytes, respectively) and Chi-square (D-F) tests are indicated: * $p<0.05$; ** $p<0.01$; ***$p<0.001$; ****$p<1e^{-9}$.

Figure 2. Nuclear morphology deteriorates faster in *baf-1(G12T)* mutants. (A-D) Morphology of hypodermal nuclei was classified on day 1 and 6 of adulthood in strains expressing GFP::LMN-1 (green) and mCh::HIS-58 (magenta) (A, B) or EMR-1::mCh (C, D). Confocal micrographs (A, C) and combined data from 4 independent experiments (B, D) are shown. Scale bars represent 10 µM (A) or 5 µM (C). Classes I-IV are defined in Materials and Methods; briefly class I corresponds to nuclei with smooth, regular NE morphology and classes II-IV represent increasingly irregular morphologies. The number of nuclei analyzed, and statistical tests are reported in Supplementary Table S1. (E, F) Quantification of GFP::LMN-1 (E) and EMR-1::mCh (F) signal in

871 the NE, nucleoplasm and cytoplasm of hypodermal cells. Data from 3 independent experiments;
872 at least 15 animals were analyzed for each strain. In these and subsequent boxplots, the midline
873 represents the median and the upper and lower limits of the box correspond to the third and
874 first quartile, respectively. The whiskers extend to the lowest and higher observations but
875 maximum up to 1.5 times the interquartile range. P values from two-sided t-tests are indicated:
876 * $p<0.05$; ** $p<0.01$.

877 **Figure 3. *baf-1(G12T)* worms are hypersensitive to GFP tagging.** (A, C) Embryonic lethality was
878 quantified for hermaphrodites carrying combinations of *baf-1(G12T)* and *gfp::lmn-1(yc32)* as
879 indicated (A) or either wild-type (+), GFP::BAF-1 (GFP) or GFP::BAF-1(G12T) (GFP::G12T) (C). Each
880 symbol represents the average per 3-5 worms. (B, D) Selected time points from confocal
881 timelapse recordings of early embryos expressing GFP::LMN-1 (green) and mCh::HIS-58
882 (magenta) (B) or either BAF-1 or BAF-1(G12T) tagged endogenously with GFP (D). Arrowheads
883 and arrows indicate abnormal (pro-)NEs and failures in chromosome segregation, respectively.
884 Time is indicated relative to P0 anaphase onset. Scale bars represent 10 µM. (E) Quantification
885 of GFP::BAF-1 (blue; n=9 adult hermaphrodites) and GFP::BAF-1(G12T) (red; n = 7) intensity at
886 the NE of hypodermal nuclei, in the nucleoplasm and in the cytoplasm. The ratio between the
887 nuclear and cytoplasmic compartment is shown in the insert. P value from two-sided t-test is
888 indicated: * $p<0.05$. Data from 3 independent experiments.

889 **Figure 4. Identification of tissue-specific BAF-1 and BAF-1(G12T) chromatin association.** (A)
890 Genome browser views of normalized GFP::Dam reads per 2 kb bins. The genes *mua-6* and *dod-*
891 *3*, which are expressed in hypodermis and intestine, respectively, are indicated. (B, C)
892 Normalized log2 values of Dam::BAF-1/GFP::Dam and Dam::BAF-1(G12T)/GFP::Dam ratios per
893 10 kb bins shown as genome browser view of chrII (B) and as box plots for all autosomes (C).
894 Grey bars above each track indicate enriched association to BAF-1 or BAF-1(G12T) (FDR < 0.05).
895 Chromosome arms were grouped based on the presence or absence of meiotic pairing centers
896 (PCs). P values from pairwise Wilcoxon Rank Sum Tests corrected for multiple testing (Benjamini
897 and Hochberg method): * $p<0.05$; ** $p<0.01$; ***$p<0.001$; ****$p<1e^{-9}$. For clarity, only selected
898 pairwise p values are indicated. (D) Normalized log2 values of Dam::BAF-1/GFP::Dam and
899 Dam::BAF-1(G12T)/GFP::Dam ratios per 2 kb bins shown as genome browser view of 500 kb
900 region from left arm of chrIII. Examples of regions enriched for association to either BAF-1 or
901 BAF-1(G12T) in the hypodermis are outlines with dashed boxed. (E, F) Venn diagram
902 representation (E) and Tissue Enrichment Analysis (F) of genes associated with BAF-1 or BAF-
903 1(G12T) in hypodermis or intestine. Total number of genes for each condition is shown in bracket
904 in E. The size and color of the circles in F reflect number of genes and p values adjusted for
905 multiple comparisons (Benjamini and Hochberg method; Q value), respectively.

906 **Figure 5. Identification of differentially expressed genes.** (A, B) Distribution of log2 values of
907 Dam::BAF-1/GFP::Dam and Dam::BAF-1(G12T)/GFP::Dam ratios per gene in hypodermis (A) and
908 intestine (B). Genes were separated in 4 categories: expressed in hypodermis and intestine (Hyp
909 & Int; 491 genes), hypodermis only (Hyp only; 1469 genes), intestine only (Int only; 1094) or not
910 detected as expressed by RAPID in any of the two tissues (Not expressed; 43330 genes). P values
911 from pairwise Wilcoxon Rank Sum Tests corrected for multiple testing (Benjamini and Hochberg
912 method) were $<2e^{-14}$ for all comparisons in the hypodermis and $<5e^{-6}$ for all comparisons in the
913 intestine. (C, D) Gene expression determined by RAPID in wild-type (x-axis) versus *baf-1(G12T)*
914 (y axis) in hypodermis (C) and intestine (D). Genes outside the dashed lines have average
915 differential log2 values >1 between the wild-type and the mutant (fold change >2). Genes
916 detected as differentially expressed in both replicas are indicated in blue (Genes up in *baf-*
917 *1(G12T)*) and red (Genes down in *baf-1(G12T)*). (E) Significant gene ontology terms identified
918 among differentially expressed genes (DEG), all combined, but also upregulated and
919 downregulated separately. The size and color of the circles reflect the number of DEGs and p

920 values adjusted for multiple comparisons (Benjamini and Hochberg method; Q value),
921 respectively.

922 **Figure 6. Differentially expressed genes bind distinctively to BAF-1 and BAF-1(G12T).** (A-B)
923 Genes with increased (A) or decreased (B) expression in intestine of *baf-1(G12T)* mutants were
924 analyzed for association to wild-type BAF-1 and BAF-1(G12T) in scatter plots (left; BAF-1
925 association on x axis; BAF-1(G12T) association on y axis) and box plots (right). Genes with
926 significantly higher association to Dam::BAF-1 or Dam::BAF-1(G12T) than to GFP::Dam are
927 indicated in red in scatter plots. Genes indicated in orange encode structural constituents of
928 ribosomes. Genes plotted in green are also deregulated in hypodermis (see **Supplementary**
929 **Figure S10**). (C) The association of differentially expressed genes encoding structural
930 constituents of ribosomes to BAF-1 and BAF-1(G12T) in intestine. P values from two-sided paired
931 t-tests, excluding outliers in A-B, are indicated.

932 **Figure 7. Altered stress resistance on *baf-1(G12T)* mutants.** (A) Survival of young adult
933 hermaphrodites as function of exposure time to 6 mM tert-Butyl hydroperoxide. Numbers in
934 brackets indicate the number of animals analysed. (B) Percentage of embryos developing into
935 larvae after exposure of young adult hermaphrodites to either 0 (left) or 25 (right) J/m^2 dose of
936 UV light. Each point represents an independent replica (n=8). (C) Survival of young adult
937 hermaphrodites as function of incubation time at 35°C. Numbers in brackets indicate the
938 number of animals analysed. P values from Chi-squared tests (A, C) and two-sided paired t-test
939 (B) are indicated.

940 **Supplementary Figure S1. *baf-1(G12T)* mutants have normal viability and lifespan at 20°C.** (A)
941 The predicted 3-dimensional structure of *C. elegans* BAF-1 (rainbow-colored; Uniprot Q03565)
942 was superimposed onto the structure of human BAF (magenta; Uniprot O75531) using iCn3D
943 Structure Viewer (Wang et al. 2022) (https://www.ncbi.nlm.nih.gov/Structure/icn3d/). Residue
944 12 is highlighted in green. (B, C) The egg laying rate (B) and embryonic viability (C) were
945 determined for hermaphrodites grown at 20°C, 25°C or shifted from 20°C to 25°C when reaching
946 adulthood. (D) Lifespan assay of wild-type and *baf-1(G12T)* hermaphrodites at 20°C. The number
947 of animals analyzed is indicated in brackets. P values from two-sided t-test (B) and Chi-square
948 test (D) are indicated: ***p<0.001.

949 **Supplementary Figure S2. Sperm defect caused by *baf-1(G12T)* mutation.** (A) Progeny
950 produced at 25°C by day 1 wild-type and *baf-1(G12T)* adults either unmated or mated with wild-
951 type or *baf-1(G12T)* males as indicated. (B, C) Total (B) and daily (C) brood size produced at 25°C
952 by feminized *fog-2* animals mated with either *fog-2* or *baf-1(G12T)* males. Error bars represent
953 standard deviation. P values from two-sided t-test are indicated: * p<0.05; ** p<0.01;
954 ***p<0.001.

955 **Supplementary Figure S3. BAF-1 and BAF-1(G12T) but not LMN-1 nor EMR-1 are present in**
956 **mature sperm.** Confocal micrographs of males (A, E) and hermaphrodites (B-D, F) expressing
957 fluorescent proteins as indicated. Animals were wild-type for *baf-1*, except *baf-1(G12T)* in C and
958 F. Spermathecae of hermaphrodites and gonads of males are outlined; arrows indicate examples
959 of sperm.

960 **Supplementary Figure S4. Nuclear morphology deteriorates faster in *baf-1(G12T)* mutants.** (A-
961 D) Morphology of hypodermal nuclei was classified on day 8 of adulthood in strains expressing
962 GFP::LMN-1 (green) and mCh::HIS-58 (magenta) (A, B) or EMR-1:.mCh (C, D). Confocal
963 micrographs (A, C) and combined data from 4 independent experiments (B, D) are shown. Scale
964 bars represent 10 µM (A) or 5 µM (C). Classes I-IV are defined in Materials and Methods; briefly,
965 class I corresponds to nuclei with smooth, regular NE morphology and classes II-IV represent
966 increasingly irregular morphologies. The number of nuclei analyzed, and statistical tests are
967 reported in Supplementary Table S1. (E-F) Quantitative RT-PCR was performed on whole-animal
968 RNA from WT and *baf-1(G12T)* animals. (E) Average Cq values for the control genes *tba-1*, *pmp-*

969 *3* and Y45F10D.4 (Zhang et al. 2012). (F) Expression of *baf-1/baf-1(G12T)*, *lmn-1* and *emr-1*
970 relative to *tba-1*. Error bars in (E-F) represent standard deviation.

971 **Supplementary Figure S5. Nuclear envelope accumulation of LMN-1 is decreased in *baf-***
972 ***1(G12T)* mutants.** Quantification of GFP::LMN-1 (A-C) and EMR-1::mCh (D-F) signal in the NE,
973 nucleoplasm and cytoplasm of intestinal and hypodermal cells at 20°C and 25°C as indicated.
974 Data from 3 independent experiments; at least 15 animals were analyzed for each strain. P
975 values from two-sided t-tests are indicated: * p<0.05; ** p<0.01; ***p<0.001.

976 **Supplementary Figure S6. *baf-1(G12T)* worms are hypersensitive to GFP tagging of LMN-1.** (A)
977 Embryonic lethality was quantified for hermaphrodites carrying combinations of *baf-1(G12T)*
978 and *gfp::lmn-1(jf98)* as indicated. Each symbol represents the average per 3-5 worms. (B)
979 Selected time points from confocal timelapse recording of 1 control and 3 *baf-1(G12T)* embryos
980 expressing endogenously tagged GFP::LMN-1 (green; allele *yc32*) and mCh::HIS-58 (magenta).
981 Arrows indicate failures in chromosome segregation. Scale bars represent 10 µM.

982 **Supplementary Figure S7. *baf-1(G12T)* worms are hypersensitive to GFP tagging.** (A) Selected
983 time points from confocal timelapse recording of 2 GFP::BAF-1 and 2 GFP::BAF-1(G12T)
984 endogenously tagged embryos co-expressing mCh::HIS-58 (magenta). Arrows indicate failures
985 in chromosome segregation. Scale bars represent 10 µM. (B) Confocal micrographs of
986 hermaphrodites expressing endogenously tagged GFP::BAF-1 or GFP::BAF-1(G12T) as indicated.

987 **Supplementary Figure S8. Chromatin accessibility is unaffected in *baf-1(G12T)* mutants.** (A)
988 Spearman correlation values for individual GFP::Dam samples with reads binned in 2 kb regions.
989 Note that the 2 tissues (hypodermis = hyp; intestine = int) cluster separately and, within each
990 tissue, the correlations between wild-type and *baf-1(G12T)* are higher than the correlations
991 between the three replicas. (B) Genome browser views of normalized GFP::Dam reads per 2 kb
992 bins for chrII.

993 **Supplementary Figure S9. Variation in BAF-1 chromatin association is higher between tissues**
994 **than between wild-type BAF-1 and mutant BAF-1(G12T).** (A) Pearson correlation values for log2
995 values (Dam::BAF-1/GFP::Dam or Dam::BAF-1(G12T)/GFP::Dam) binned in 100 kb regions. Note
996 that the 2 tissues (hypodermis = hyp; intestine = int) cluster separately and, within each tissue,
997 the correlations between wild-type and *baf-1(G12T)* are higher than the correlations between
998 the three replicas. (B, C) Normalized log2 values of Dam::BAF-1/GFP::Dam and Dam::BAF-
999 1(G12T)/GFP::Dam ratios per 100 kb bins for the entire genome (B) and per 2 kb bins as genome
1000 browser view of 500 kb region from left arm of chrI (C). For clarity, the curves in B represent
1001 rolling means across 3 consecutive bins. Grey bars above each track in C indicate enriched
1002 association to BAF-1 or BAF-1(G12T) (FDR < 0.05). Examples of regions enriched for association
1003 to either BAF-1 or BAF-1(G12T) in the intestine are outlines with dashed boxed.

1004 **Supplementary Figure S10. Differentially expressed genes encoding cuticle components bind**
1005 **distinctively to BAF-1 and BAF-1(G12T).** (A-B) Genes with increased (A) or decreased (B)
1006 expression in hypodermis of *baf-1(G12T)* mutants were analyzed for association to wild-type
1007 BAF-1 (x axis) and BAF-1(G12T) in scatter plots (left; BAF-1 association on x axis; BAF-1(G12T)
1008 association on y axis) and box plots (right). Genes with significantly higher association to
1009 Dam::BAF-1 or Dam::BAF-1(G12T) than to GFP::Dam are indicated in red in scatter plots. Genes
1010 indicated in orange (and *col-63* indicated in red) encode structural constituents of the cuticle.
1011 Genes plotted in green are also deregulated in intestine (see **Figure 6**). (C) The association of
1012 differentially expressed genes encoding structural constituents of the cuticle to BAF-1 and BAF-
1013 1(G12T) in hypodermis. P values from two-sided paired t-tests, excluding outliers in A-B, are
1014 indicated.

1015 **Supplementary Video S1. Abnormal localization of GFP::LMN-1 and chromosome segregation**
1016 **defects caused by *baf-1(G12T)*.** Control (left) and *baf-1(G12T)* (right) embryos expressing
1017 GFP::LMN-1 (green) and mCh::HIS-58 (magenta) were observed by spinning disk confocal

1018 microscopy every 12.5 sec. Each time point represents maximum projections of 17 confocal
1019 slices. Corresponds to Figure 3B.

1020 **Supplementary Video S2. Abnormal localization of GFP::BAF-1(G12T) and chromosome**
1021 **segregation defects caused by *baf-1(G12T)*.** Control GFP::BAF-1 (left) and GFP::BAF-1(G12T)
1022 (right) embryos co-expressing mCh::HIS-58 (magenta; GFP in green) were observed by spinning
1023 disk confocal microscopy every 20.4 sec. Each time point represents maximum projections of 17
1024 confocal slices. Corresponds to Figure 3D.

1025

1026 **REFERENCES:**

1027 Ahringer J, Gasser SM. 2018. Repressive Chromatin in Caenorhabditis elegans: Establishment,
1028 Composition, and Function. *Genetics* **208**: 491-511.
1029 Angeles-Albores D, Lee R, Chan J, Sternberg P. 2018. Two new functions in the WormBase
1030 Enrichment Suite. *MicroPubl Biol* **2018**.
1031 Angeles-Albores D, RY NL, Chan J, Sternberg PW. 2016. Tissue enrichment analysis for C. elegans
1032 genomics. *BMC Bioinformatics* **17**: 366.
1033 Arantes-Oliveira N, Apfeld J, Dillin A, Kenyon C. 2002. Regulation of life-span by germ-line stem
1034 cells in Caenorhabditis elegans. *Science* **295**: 502-505.
1035 Arribere JA, Bell RT, Fu BX, Artiles KL, Hartman PS, Fire AZ. 2014. Efficient marker-free recovery
1036 of custom genetic modifications with CRISPR/Cas9 in Caenorhabditis elegans. *Genetics*
1037 **198**: 837-846.
1038 Asencio C, Davidson IF, Santarella-Mellwig R, Ly-Hartig TB, Mall M, Wallenfang MR, Mattaj IW,
1039 Gorjanacz M. 2012. Coordination of kinase and phosphatase activities by Lem4 enables
1040 nuclear envelope reassembly during mitosis. *Cell* **150**: 122-135.
1041 Bardou P, Mariette J, Escudie F, Djemiel C, Klopp C. 2014. jvenn: an interactive Venn diagram
1042 viewer. *BMC Bioinformatics* **15**: 293.
1043 Barger SR, Penfield L, Bahmanyar S. 2023. Nuclear envelope assembly relies on CHMP-7 in the
1044 absence of BAF-LEM-mediated hole closure. *J Cell Sci* **136**.
1045 Beanan MJ, Strome S. 1992. Characterization of a germ-line proliferation mutation in C. elegans.
1046 *Development* **116**: 755-766.
1047 Berman JR, Kenyon C. 2006. Germ-cell loss extends C. elegans life span through regulation of
1048 DAF-16 by kri-1 and lipophilic-hormone signaling. *Cell* **124**: 1055-1068.
1049 Bone CR, Chang YT, Cain NE, Murphy SP, Starr DA. 2016. Nuclei migrate through constricted
1050 spaces using microtubule motors and actin networks in C. elegans hypodermal cells.
1051 *Development* **143**: 4193-4202.
1052 Bradley CM, Ronning DR, Ghirlando R, Craigie R, Dyda F. 2005. Structural basis for DNA bridging
1053 by barrier-to-autointegration factor. *Nat Struct Mol Biol* **12**: 935-936.
1054 Breusegem SY, Houghton J, Romero-Bueno R, Fragoso-Luna A, Kentistou KA, Ong KK, Janssen A,
1055 Bright NA, Riedel CG, Perry JRB et al. 2022. A multiparametric anti-aging CRISPR screen
1056 uncovers a role for BAF in protein translation. *bioRxiv* doi:10.1101/2022.10.07.509469.
1057 Brueckner L, Zhao PA, van Schaik T, Leemans C, Sima J, Peric-Hupkes D, Gilbert DM, van Steensel
1058 B. 2020. Local rewiring of genome-nuclear lamina interactions by transcription. *EMBO J*
1059 **39**: e103159.
1060 Cabanillas R, Cadinanos J, Villameytide JA, Perez M, Longo J, Richard JM, Alvarez R, Duran NS,
1061 Illan R, Gonzalez DJ et al. 2011. Nestor-Guillermo progeria syndrome: a novel premature
1062 aging condition with early onset and chronic development caused by BANF1 mutations.
1063 *Am J Med Genet A* **155A**: 2617-2625.
1064 Cabianca DS, Munoz-Jimenez C, Kalck V, Gaidatzis D, Padeken J, Seeber A, Askjaer P, Gasser SM.
1065 2019. Active chromatin marks drive spatial sequestration of heterochromatin in C.
1066 elegans nuclei. *Nature* **569**: 734-739.

1067 Collins JJ, Huang C, Hughes S, Kornfeld K. 2008. The measurement and analysis of age-related
1068 changes in Caenorhabditis elegans. *WormBook* doi:10.1895/wormbook.1.137.1: 1-21.
1069 Cox JL, Mallanna SK, Ormsbee BD, Desler M, Wiebe MS, Rizzino A. 2011. Banf1 is required to
1070 maintain the self-renewal of both mouse and human embryonic stem cells. *J Cell Sci* **124**:
1071 2654-2665.
1072 de la Cruz Ruiz P, Romero-Bueno R, Askjaer P. 2022. Analysis of Nuclear Pore Complexes in
1073 Caenorhabditis elegans by Live Imaging and Functional Genomics. *Methods Mol Biol*
1074 **2502**: 161-182.
1075 Dickinson DJ, Ward JD, Reiner DJ, Goldstein B. 2013. Engineering the Caenorhabditis elegans
1076 genome using Cas9-triggered homologous recombination. *Nat Methods* **10**: 1028-1034.
1077 Dobrzynska A, Askjaer P, Gruenbaum Y. 2016a. Lamin-Binding Proteins in Caenorhabditis
1078 elegans. *Methods in enzymology* **569**: 455-483.
1079 Dobrzynska A, Gonzalo S, Shanahan C, Askjaer P. 2016b. The nuclear lamina in health and
1080 disease. *Nucleus* **7**: 233-248.
1081 Donadille B, D'Anella P, Auclair M, Uhrhammer N, Sorel M, Grigorescu R, Ouzounian S, Cambonie
1082 G, Boulot P, Laforet P et al. 2013. Partial lipodystrophy with severe insulin resistance
1083 and adult progeria Werner syndrome. *Orphanet J Rare Dis* **8**: 106.
1084 Duan T, Thyagarajan S, Amoiroglou A, Rogers GC, Geyer PK. 2023. Analysis of a rare progeria
1085 variant of Barrier-to-autointegration factor in Drosophila connects centromere function
1086 to tissue homeostasis. *Cell Mol Life Sci* **80**: 73.
1087 Fisher HG, Patni N, Scheuerle AE. 2020. An additional case of Nestor-Guillermo progeria
1088 syndrome diagnosed in early childhood. *Am J Med Genet A* **182**: 2399-2402.
1089 Fragoso-Luna A, Askjaer P. 2023. The Nuclear Envelope in Ageing and Progeria. *Subcell Biochem*
1090 **102**: 53-75.
1091 Fragoso-Luna A, Romero-Bueno R, Eibl M, Ayuso C, Munoz-Jimenez C, Benes V, Cases I, Askjaer
1092 P. 2023. Expanded FLP toolbox for spatiotemporal protein degradation and
1093 transcriptomic profiling in Caenorhabditis elegans. *Genetics* **223**.
1094 Friedland AE, Tzur YB, Esvelt KM, Colaiacovo MP, Church GM, Calarco JA. 2013. Heritable
1095 genome editing in C. elegans via a CRISPR-Cas9 system. *Nat Methods* **10**: 741-743.
1096 Frøkjær-Jensen C, Davis MW, Ailion M, Jorgensen EM. 2012. Improved Mos1-mediated
1097 transgenesis in C. elegans. *Nat Methods* **9**: 117-118.
1098 Frøkjær-Jensen C, Davis MW, Hopkins CE, Newman BJ, Thummel JM, Olesen SP, Grunnet M,
1099 Jorgensen EM. 2008. Single-copy insertion of transgenes in Caenorhabditis elegans. *Nat*
1100 *Genet* **40**: 1375-1383.
1101 Furukawa K, Sugiyama S, Osouda S, Goto H, Inagaki M, Horigome T, Omata S, McConnell M,
1102 Fisher PA, Nishida Y. 2003. Barrier-to-autointegration factor plays crucial roles in cell
1103 cycle progression and nuclear organization in Drosophila. *J Cell Sci* **116**: 3811-3823.
1104 Gerstein MB Lu ZJ Van Nostrand EL Cheng C Arshinoff BI Liu T Yip KY Robilotto R Rechtsteiner A
1105 Ikegami K et al. 2010. Integrative analysis of the Caenorhabditis elegans genome by the
1106 modENCODE project. *Science* **330**: 1775-1787.
1107 Gomez-Saldivar G, Osuna-Luque J, Semple JI, Glauser DA, Jarriault S, Meister P. 2020. Tissue-
1108 Specific Transcription Footprinting Using RNA PoI DamID (RAPID) in Caenorhabditis
1109 elegans. *Genetics* doi:10.1534/genetics.120.303774.
1110 Gonzalez-Aguilera C, Ikegami K, Ayuso C, de Luis A, Iniguez M, Cabello J, Lieb JD, Askjaer P. 2014.
1111 Genome-wide analysis links emerin to neuromuscular junction activity in Caenorhabditis
1112 elegans. *Genome Biol* **15**: R21.
1113 Gonzalo S, Kreienkamp R, Askjaer P. 2017. Hutchinson-Gilford Progeria Syndrome: A premature
1114 aging disease caused by LMNA gene mutations. *Ageing Res Rev* **33**: 18-29.
1115 Gorjanacz M, Klerkx EP, Galy V, Santarella R, Lopez-Iglesias C, Askjaer P, Mattaj IW. 2007.
1116 Caenorhabditis elegans BAF-1 and its kinase VRK-1 participate directly in post-mitotic
1117 nuclear envelope assembly. *EMBO J* **26**: 132-143.

1118 Haithcock E, Dayani Y, Neufeld E, Zahand AJ, Feinstein N, Mattout A, Gruenbaum Y, Liu J. 2005.
1119 Age-related changes of nuclear architecture in Caenorhabditis elegans. *Proc Natl Acad*
1120 *Sci U S A* **102**: 16690-16695.
1121 Halfmann CT, Sears RM, Katiyar A, Busselman BW, Aman LK, Zhang Q, O'Bryan CS, Angelini TE,
1122 Lele TP, Roux KJ. 2019. Repair of nuclear ruptures requires barrier-to-autointegration
1123 factor. *J Cell Biol* **218**: 2136-2149.
1124 Haraguchi T, Kojidani T, Koujin T, Shimi T, Osakada H, Mori C, Yamamoto A, Hiraoka Y. 2008. Live
1125 cell imaging and electron microscopy reveal dynamic processes of BAF-directed nuclear
1126 envelope assembly. *J Cell Sci* **121**: 2540-2554.
1127 Haraguchi T, Koujin T, Segura-Totten M, Lee KK, Matsuoka Y, Yoneda Y, Wilson KL, Hiraoka Y.
1128 2001. BAF is required for emerin assembly into the reforming nuclear envelope. *J Cell*
1129 *Sci* **114**: 4575-4585.
1130 Holaska JM, Lee KK, Kowalski AK, Wilson KL. 2003. Transcriptional repressor germ cell-less (GCL)
1131 and barrier to autointegration factor (BAF) compete for binding to emerin in vitro. *J Biol*
1132 *Chem* **278**: 6969-6975.
1133 Hsin H, Kenyon C. 1999. Signals from the reproductive system regulate the lifespan of C. elegans.
1134 *Nature* **399**: 362-366.
1135 Ikegami K, Egelhofer TA, Strome S, Lieb JD. 2010. Caenorhabditis elegans chromosome arms are
1136 anchored to the nuclear membrane via discontinuous association with LEM-2. *Genome*
1137 *Biol* **11**: R120.
1138 Janssen A, Marcelot A, Breusegem S, Legrand P, Zinn-Justin S, Larrieu D. 2022. The BAF A12T
1139 mutation disrupts lamin A/C interaction, impairing robust repair of nuclear envelope
1140 ruptures in Nestor-Guillermo progeria syndrome cells. *Nucleic Acids Res*
1141 doi:10.1093/nar/gkac726.
1142 Kamath RS, Fraser AG, Dong Y, Poulin G, Durbin R, Gotta M, Kanapin A, Le Bot N, Moreno S,
1143 Sohrmann M et al. 2003. Systematic functional analysis of the Caenorhabditis elegans
1144 genome using RNAi. *Nature* **421**: 231-237.
1145 Katsanos D, Ferrando-Marco M, Razzaq I, Aughey G, Southall TD, Barkoulas M. 2021. Gene
1146 expression profiling of epidermal cell types in C. elegans using Targeted DamID.
1147 *Development* **148**.
1148 Kent WJ, Sugnet CW, Furey TS, Roskin KM, Pringle TH, Zahler AM, Haussler D. 2002. The human
1149 genome browser at UCSC. *Genome Res* **12**: 996-1006.
1150 Kind J, van Steensel B. 2014. Stochastic genome-nuclear lamina interactions: modulating roles
1151 of Lamin A and BAF. *Nucleus* **5**: 124-130.
1152 Kono Y, Adam SA, Sato Y, Reddy KL, Zheng Y, Medalia O, Goldman RD, Kimura H, Shimi T. 2022.
1153 Nucleoplasmic lamin C rapidly accumulates at sites of nuclear envelope rupture with
1154 BAF and cGAS. *J Cell Biol* **221**.
1155 Kubben N, Zhang W, Wang L, Voss TC, Yang J, Qu J, Liu GH, Misteli T. 2016. Repression of the
1156 Antioxidant NRF2 Pathway in Premature Aging. *Cell* **165**: 1361-1374.
1157 Lee MS, Craigie R. 1998. A previously unidentified host protein protects retroviral DNA from
1158 autointegration. *Proc Natl Acad Sci U S A* **95**: 1528-1533.
1159 Lin Q, Yu B, Wang X, Zhu S, Zhao G, Jia M, Huang F, Xu N, Ren H, Jiang Q et al. 2020. K6-linked
1160 SUMOylation of BAF regulates nuclear integrity and DNA replication in mammalian cells.
1161 *Proc Natl Acad Sci U S A* **117**: 10378-10387.
1162 Link J, Jantsch V. 2019. Meiotic chromosomes in motion: a perspective from Mus musculus and
1163 Caenorhabditis elegans. *Chromosoma* **128**: 317-330.
1164 Liu J, Rolef Ben-Shahar T, Riemer D, Treinin M, Spann P, Weber K, Fire A, Gruenbaum Y. 2000.
1165 Essential roles for Caenorhabditis elegans lamin gene in nuclear organization, cell cycle
1166 progression, and spatial organization of nuclear pore complexes. *Mol Biol Cell* **11**: 3937-
1167 3947.
1168 Love MI, Huber W, Anders S. 2014. Moderated estimation of fold change and dispersion for RNA-
1169 seq data with DESeq2. *Genome Biol* **15**: 550.

1170 Manzo SG, Dauban L, van Steensel B. 2022. Lamina-associated domains: Tethers and looseners.
1171 *Curr Opin Cell Biol* **74**: 80-87.
1172 Marcelot A, Petitalot A, Ropars V, Le Du MH, Samson C, Dubois S, Hoffmann G, Miron S, Cuniasse
1173 P, Marquez JA et al. 2021. Di-phosphorylated BAF shows altered structural dynamics and
1174 binding to DNA, but interacts with its nuclear envelope partners. *Nucleic Acids Res* **49**:
1175 3841-3855.
1176 Margalit A, Neufeld E, Feinstein N, Wilson KL, Podbilewicz B, Gruenbaum Y. 2007. Barrier to
1177 autointegration factor blocks premature cell fusion and maintains adult muscle integrity
1178 in C. elegans. *J Cell Biol* **178**: 661-673.
1179 Margalit A, Segura-Totten M, Gruenbaum Y, Wilson KL. 2005. Barrier-to-autointegration factor
1180 is required to segregate and enclose chromosomes within the nuclear envelope and
1181 assemble the nuclear lamina. *Proc Natl Acad Sci U S A* **102**: 3290-3295.
1182 Marshall OJ, Brand AH. 2015. damidseq_pipeline: an automated pipeline for processing DamID
1183 sequencing datasets. *Bioinformatics* **31**: 3371-3373.
1184 Molitor TP, Traktman P. 2014. Depletion of the protein kinase VRK1 disrupts nuclear envelope
1185 morphology and leads to BAF retention on mitotic chromosomes. *Mol Biol Cell* **25**: 891-
1186 903.
1187 Montes de Oca R, Shoemaker CJ, Gucek M, Cole RN, Wilson KL. 2009. Barrier-to-autointegration
1188 factor proteome reveals chromatin-regulatory partners. *PLoS One* **4**: e7050.
1189 Morales-Martinez A, Dobrzynska A, Askjaer P. 2015. Inner nuclear membrane protein LEM-2 is
1190 required for correct nuclear separation and morphology in C. elegans. *J Cell Sci* **128**:
1191 1090-1096.
1192 Munoz-Jimenez C, Ayuso C, Dobrzynska A, Torres-Mendez A, Ruiz PC, Askjaer P. 2017. An
1193 Efficient FLP-Based Toolkit for Spatiotemporal Control of Gene Expression in
1194 Caenorhabditis elegans. *Genetics* **206**: 1763-1778.
1195 Nichols RJ, Wiebe MS, Traktman P. 2006. The Vaccinia-related Kinases Phosphorylate the N'
1196 Terminus of BAF, Regulating Its Interaction with DNA and Its Retention in the Nucleus.
1197 *Mol Biol Cell* **17**: 2451-2464.
1198 Paix A, Folkmann A, Rasoloson D, Seydoux G. 2015. High Efficiency, Homology-Directed Genome
1199 Editing in Caenorhabditis elegans Using CRISPR-Cas9 Ribonucleoprotein Complexes.
1200 *Genetics* **201**: 47-54.
1201 Paquet N, Box JK, Ashton NW, Suraweera A, Croft LV, Urquhart AJ, Bolderson E, Zhang SD,
1202 O'Byrne KJ, Richard DJ. 2014. Nestor-Guillermo Progeria Syndrome: a biochemical
1203 insight into Barrier-to-Autointegration Factor 1, alanine 12 threonine mutation. *BMC*
1204 *Mol Biol* **15**: 27.
1205 Perez-Jimenez MM, Rodriguez-Palero MJ, Rodenas E, Askjaer P, Munoz MJ. 2014. Age-
1206 dependent changes of nuclear morphology are uncoupled from longevity in
1207 Caenorhabditis elegans IGF/insulin receptor daf-2 mutants. *Biogerontology* **15**: 279-288.
1208 Puente XS, Quesada V, Osorio FG, Cabanillas R, Cadinanos J, Fraile JM, Ordonez GR, Puente DA,
1209 Gutierrez-Fernandez A, Fanjul-Fernandez M et al. 2011. Exome sequencing and
1210 functional analysis identifies BANF1 mutation as the cause of a hereditary progeroid
1211 syndrome. *American journal of human genetics* **88**: 650-656.
1212 Rodenas E, Gonzalez-Aguilera C, Ayuso C, Askjaer P. 2012. Dissection of the NUP107 nuclear
1213 pore subcomplex reveals a novel interaction with spindle assembly checkpoint protein
1214 MAD1 in Caenorhabditis elegans. *Mol Biol Cell* **23**: 930-944.
1215 Samson C, Petitalot A, Celli F, Herrada I, Ropars V, Le Du MH, Nhiri N, Jacquet E, Arteni AA,
1216 Buendia B et al. 2018. Structural analysis of the ternary complex between lamin A/C,
1217 BAF and emerin identifies an interface disrupted in autosomal recessive progeroid
1218 diseases. *Nucleic Acids Res* doi:10.1093/nar/gky736.
1219 Samwer M, Schneider MWG, Hoefler R, Schmalhorst PS, Jude JG, Zuber J, Gerlich DW. 2017. DNA
1220 Cross-Bridging Shapes a Single Nucleus from a Set of Mitotic Chromosomes. *Cell* **170**:
1221 956-972 e923.

1222 Schedl T, Kimble J. 1988. fog-2, a germ-line-specific sex determination gene required for
1223 hermaphrodite spermatogenesis in Caenorhabditis elegans. *Genetics* **119**: 43-61.
1224 Schindelin J, Arganda-Carreras I, Frise E, Kaynig V, Longair M, Pietzsch T, Preibisch S, Rueden C,
1225 Saalfeld S, Schmid B et al. 2012. Fiji: an open-source platform for biological-image
1226 analysis. *Nat Methods* **9**: 676-682.
1227 Schwartz ML, Jorgensen EM. 2016. SapTrap, a Toolkit for High-Throughput CRISPR/Cas9 Gene
1228 Modification in Caenorhabditis elegans. *Genetics* **202**: 1277-1288.
1229 Sears RM, Roux KJ. 2020. Diverse cellular functions of barrier-to-autointegration factor and its
1230 roles in disease. *J Cell Sci* **133**.
1231 Sharma R, Ritler D, Meister P. 2016. Tools for DNA adenine methyltransferase identification
1232 analysis of nuclear organization during C. elegans development. *Genesis* **54**: 151-159.
1233 Shin JY, Worman HJ. 2022. Molecular Pathology of Laminopathies. *Annu Rev Pathol* **17**: 159-180.
1234 Soo SK, Rudich ZD, Ko B, Moldakozhayev A, AlOkda A, Van Raamsdonk JM. 2023. Biological
1235 resilience and aging: Activation of stress response pathways contributes to lifespan
1236 extension. *Ageing Res Rev* **88**: 101941.
1237 Southall TD, Gold KS, Egger B, Davidson CM, Caygill EE, Marshall OJ, Brand AH. 2013. Cell-type-
1238 specific profiling of gene expression and chromatin binding without cell isolation:
1239 assaying RNA Pol II occupancy in neural stem cells. *Dev Cell* **26**: 101-112.
1240 Stiernagle T. 2006. Maintenance of C. elegans. *WormBook* doi:10.1895/wormbook.1.101.1: 1-
1241 11.
1242 Stroustrup N, Ulmschneider BE, Nash ZM, Lopez-Moyado IF, Apfeld J, Fontana W. 2013. The
1243 Caenorhabditis elegans Lifespan Machine. *Nat Methods* **10**: 665-670.
1244 Swift J, Ivanovska IL, Buxboim A, Harada T, Dingal PC, Pinter J, Pajerowski JD, Spinler KR, Shin
1245 JW, Tewari M et al. 2013. Nuclear lamin-A scales with tissue stiffness and enhances
1246 matrix-directed differentiation. *Science* **341**: 1240104.
1247 Team R. 2020. RStudio: Integrated Development Environment for R. pp. RStudio, PBC.
1248 Towbin BD, Gonzalez-Aguilera C, Sack R, Gaidatzis D, Kalck V, Meister P, Askjaer P, Gasser SM.
1249 2012. Step-Wise Methylation of Histone H3K9 Positions Heterochromatin at the Nuclear
1250 Periphery. *Cell* **150**: 934-947.
1251 Turgay Y, Eibauer M, Goldman AE, Shimi T, Khayat M, Ben-Harush K, Dubrovsky-Gaupp A, Sapra
1252 KT, Goldman RD, Medalia O. 2017. The molecular architecture of lamins in somatic cells.
1253 *Nature* **543**: 261-264.
1254 Ungricht R, Kutay U. 2017. Mechanisms and functions of nuclear envelope remodelling. *Nat Rev*
1255 *Mol Cell Biol* doi:10.1038/nrm.2016.153.
1256 Unnikannan CP, Reuveny A, Grunberg D, Volk T. 2020. Recruitment of BAF to the nuclear
1257 envelope couples the LINC complex to endoreplication. *Development* **147**.
1258 Vogel C, Marcotte EM. 2012. Insights into the regulation of protein abundance from proteomic
1259 and transcriptomic analyses. *Nat Rev Genet* **13**: 227-232.
1260 Wang J, Youkharibache P, Marchler-Bauer A, Lanczycki C, Zhang D, Lu S, Madej T, Marchler GH,
1261 Cheng T, Chong LC et al. 2022. iCn3D: From Web-Based 3D Viewer to Structural Analysis
1262 Tool in Batch Mode. *Front Mol Biosci* **9**: 831740.
1263 Wang S, Stoops E, Cp U, Markus B, Reuveny A, Ordan E, Volk T. 2018. Mechanotransduction via
1264 the LINC complex regulates DNA replication in myonuclei. *J Cell Biol* **217**: 2005-2018.
1265 Ward JD. 2015. Rapid and Precise Engineering of the Caenorhabditis elegans Genome with
1266 Lethal Mutation Co-Conversion and Inactivation of NHEJ Repair. *Genetics* **199**: 363-377.
1267 Wolf N, Hirsh D, McIntosh JR. 1978. Spermatogenesis in males of the free-living nematode,
1268 Caenorhabditis elegans. *J Ultrastruct Res* **63**: 155-169.
1269 Yamamoto S, Kanca O, Wangler MF, Bellen HJ. 2024. Integrating non-mammalian model
1270 organisms in the diagnosis of rare genetic diseases in humans. *Nat Rev Genet* **25**: 46-60.
1271 Young AM, Gunn AL, Hatch EM. 2020. BAF facilitates interphase nuclear membrane repair
1272 through recruitment of nuclear transmembrane proteins. *Mol Biol Cell* **31**: 1551-1560.

1273 Zhang Y, Chen D, Smith MA, Zhang B, Pan X. 2012. Selection of reliable reference genes in
1274 Caenorhabditis elegans for analysis of nanotoxicity. *PLoS One* **7**: e31849.
1275 Zheng R, Ghirlando R, Lee MS, Mizuuchi K, Krause M, Craigie R. 2000. Barrier-to-autointegration
1276 factor (BAF) bridges DNA in a discrete, higher-order nucleoprotein complex. *Proc Natl*
1277 *Acad Sci U S A* **97**: 8997-9002.
1278

Figure 1

A

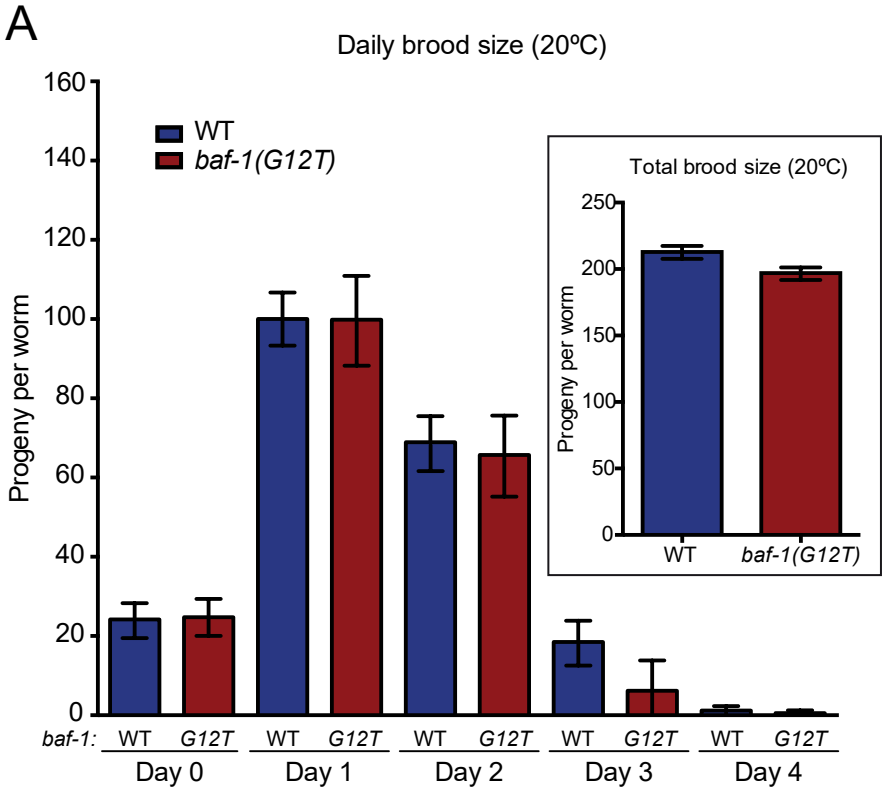

B

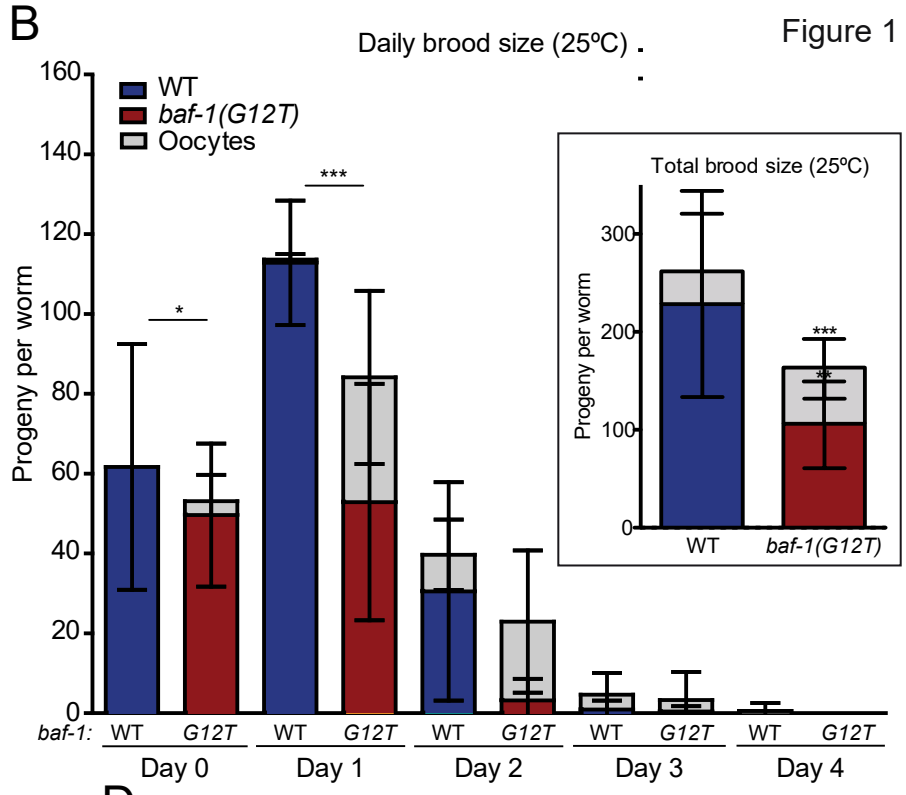

C

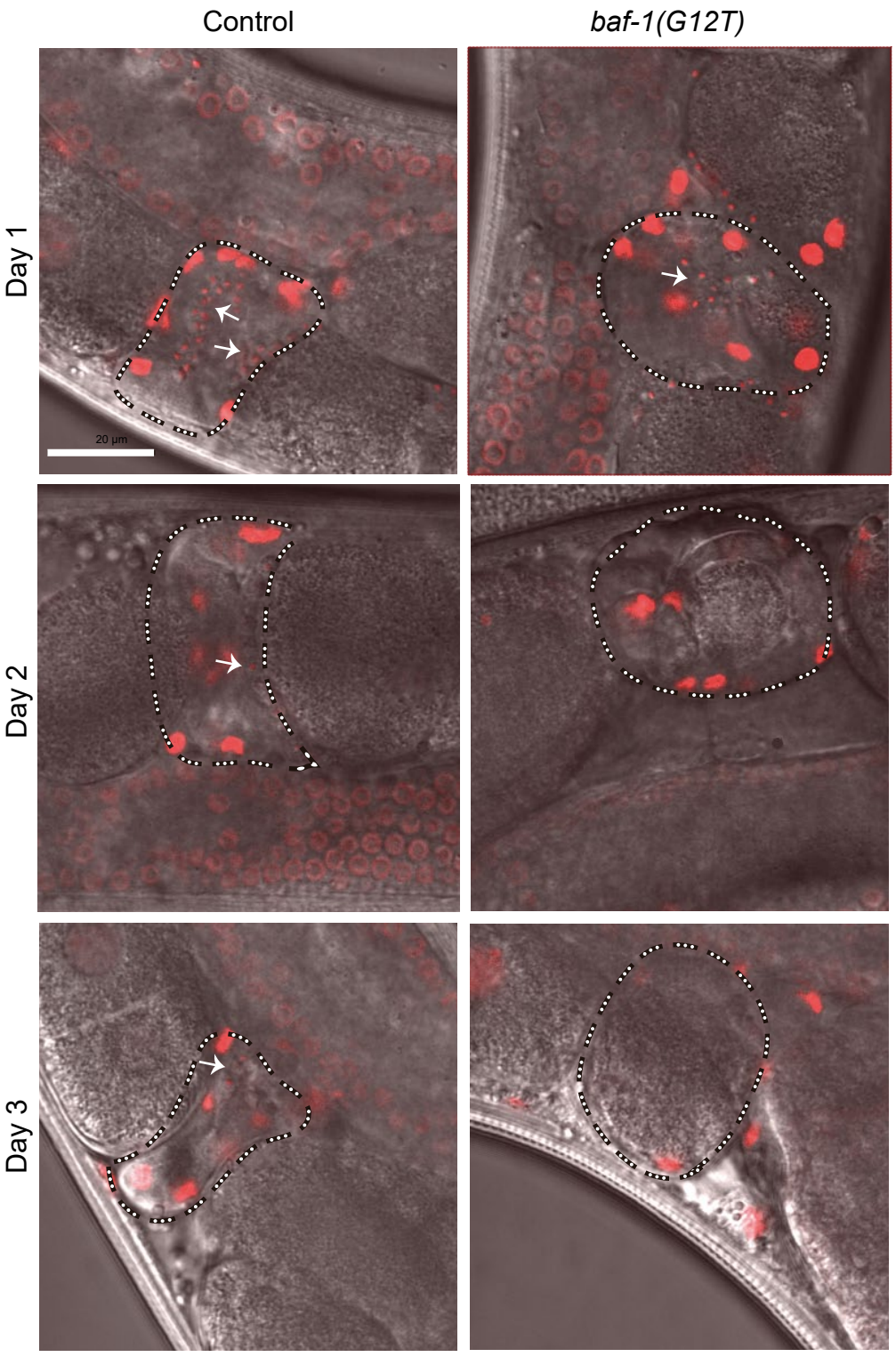

D

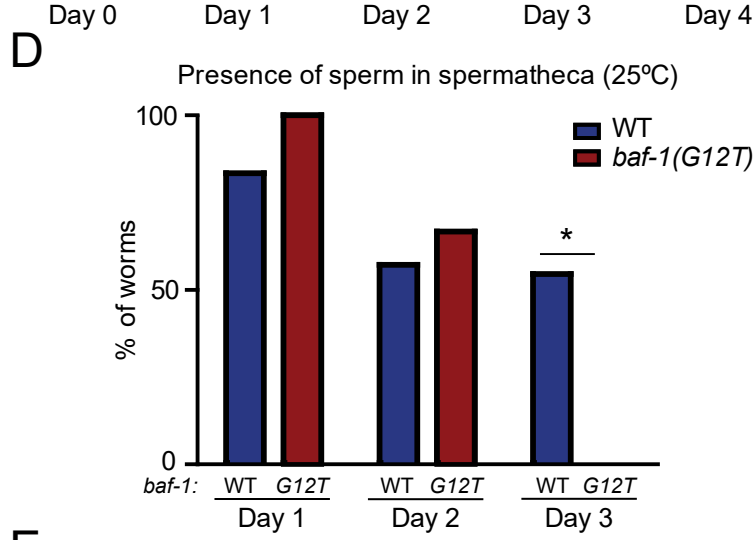

E

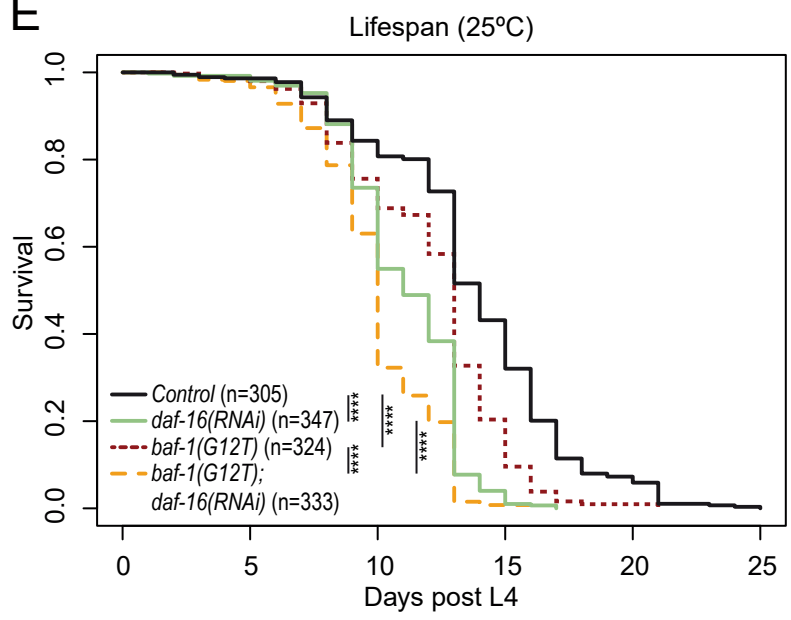

F

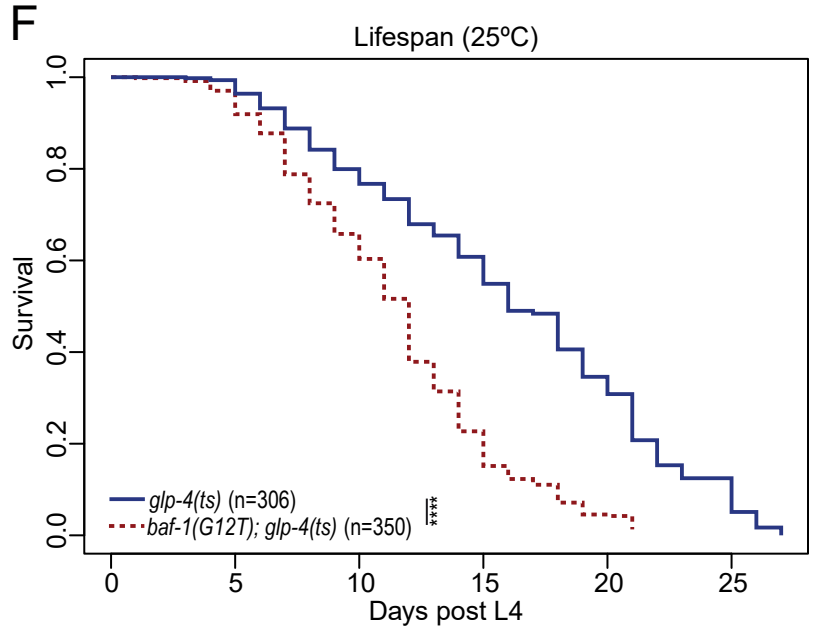

Figure 2

A

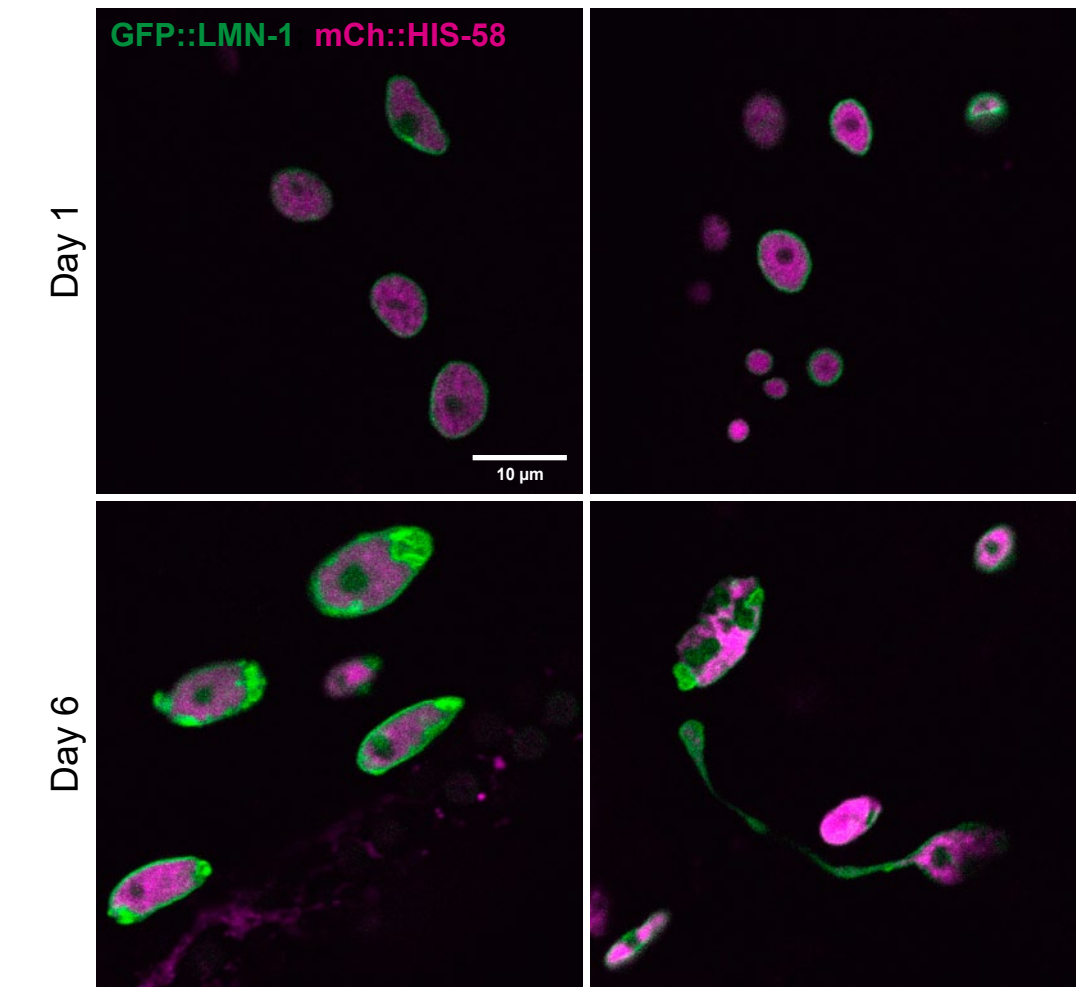

B

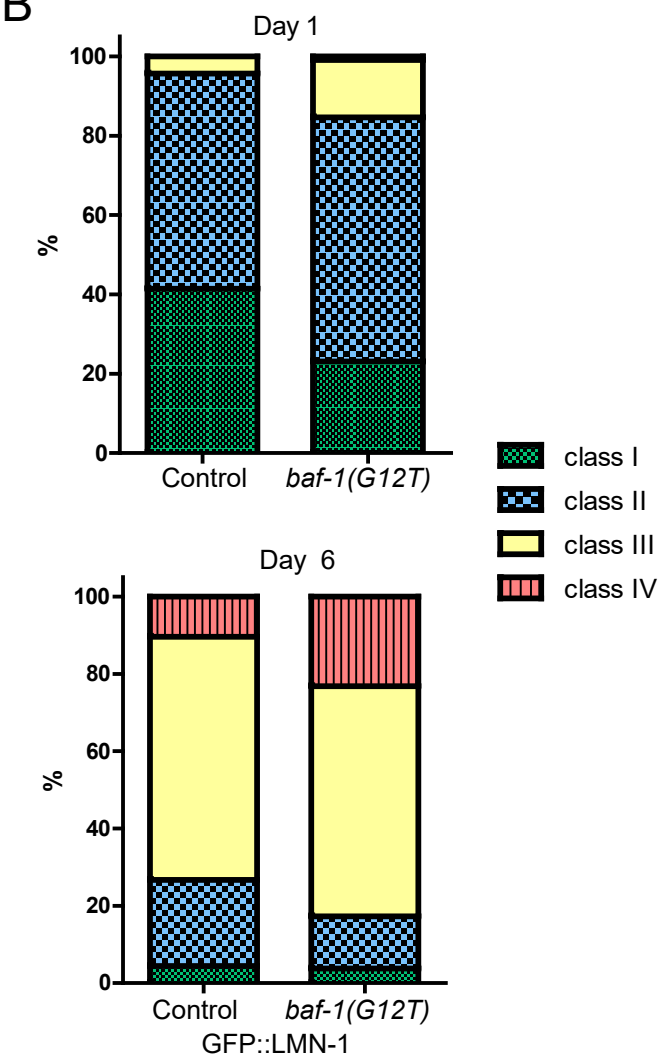

C

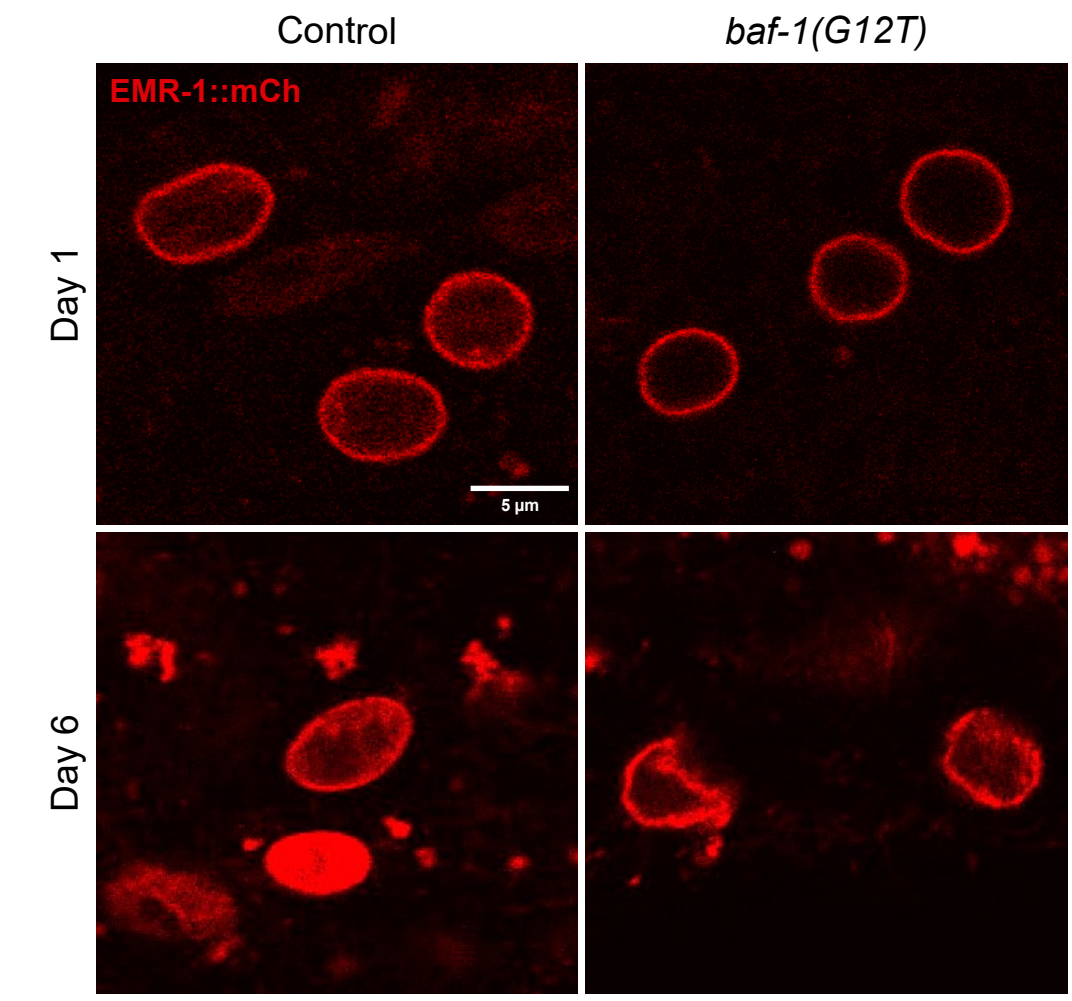

D

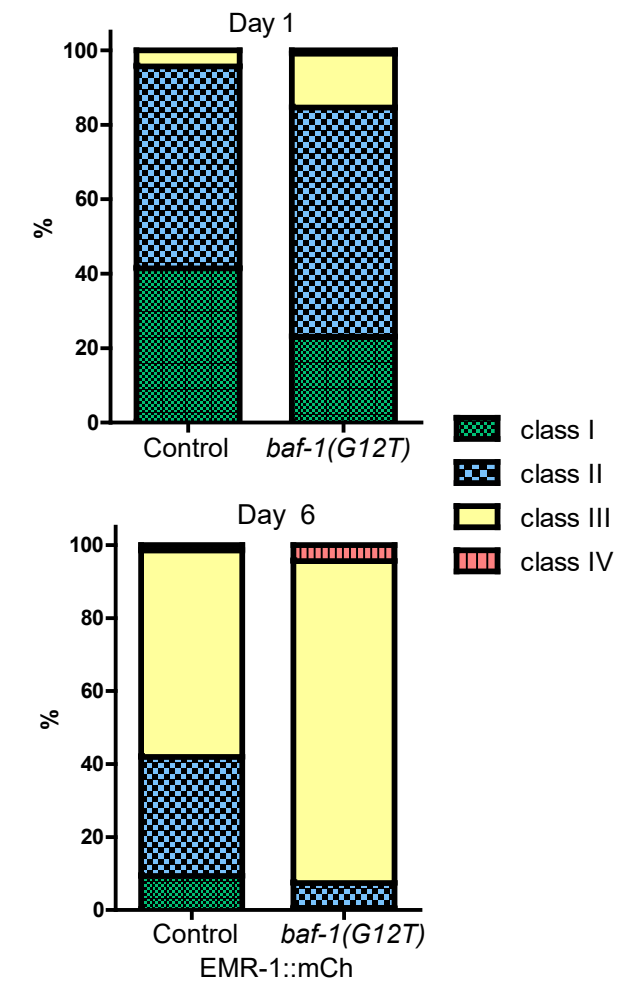

E

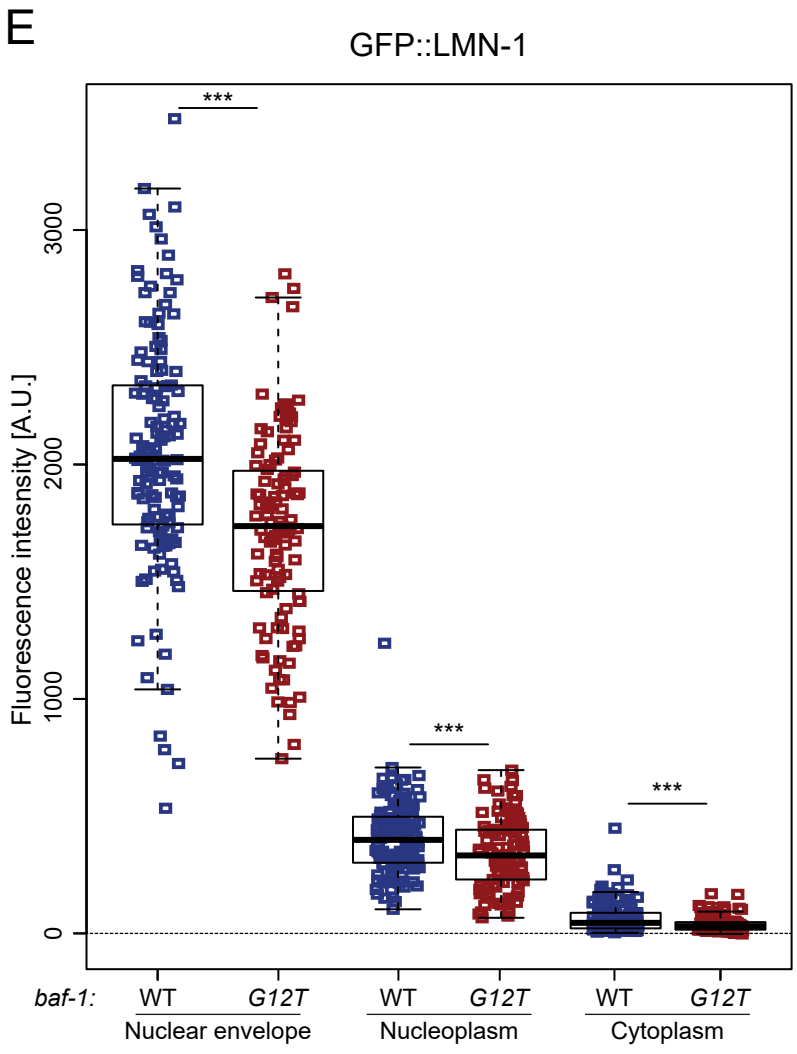

F

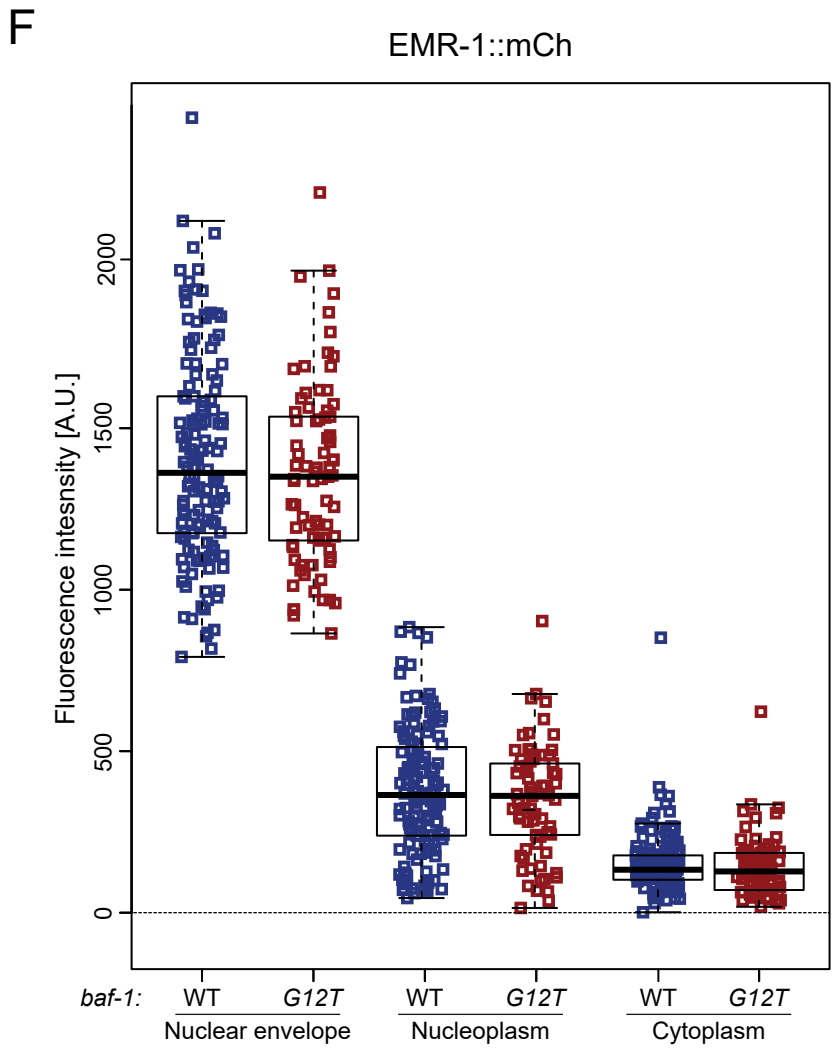

Figure 3

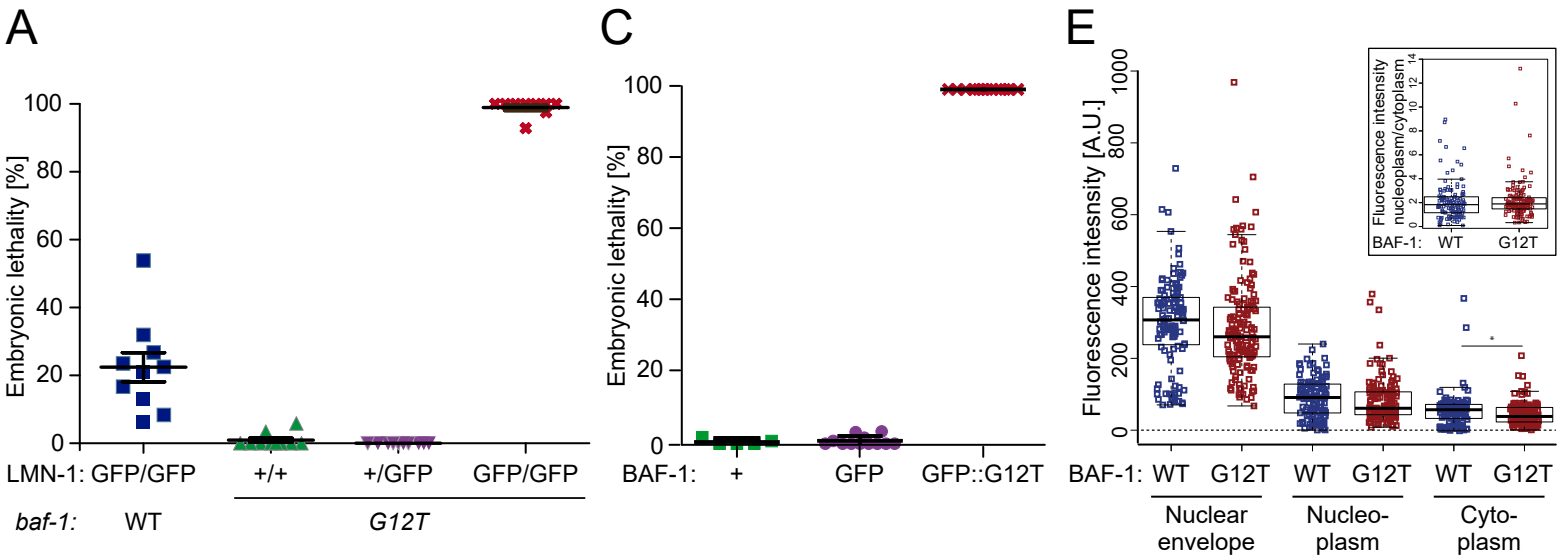

B

mCh::HIS-58 ; GFP::LMN-1

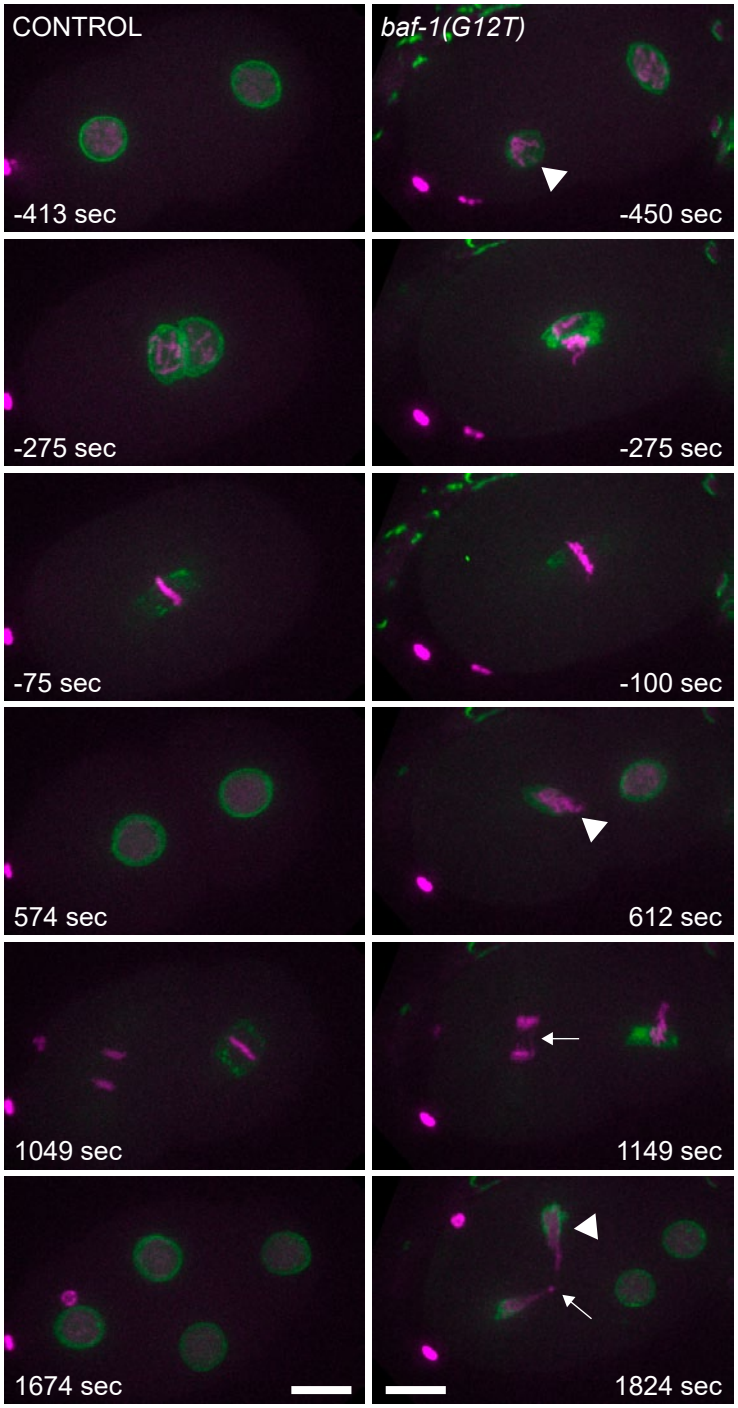

D

mCh::HIS-58 ; GFP::BAF-1 (WT/G12T)

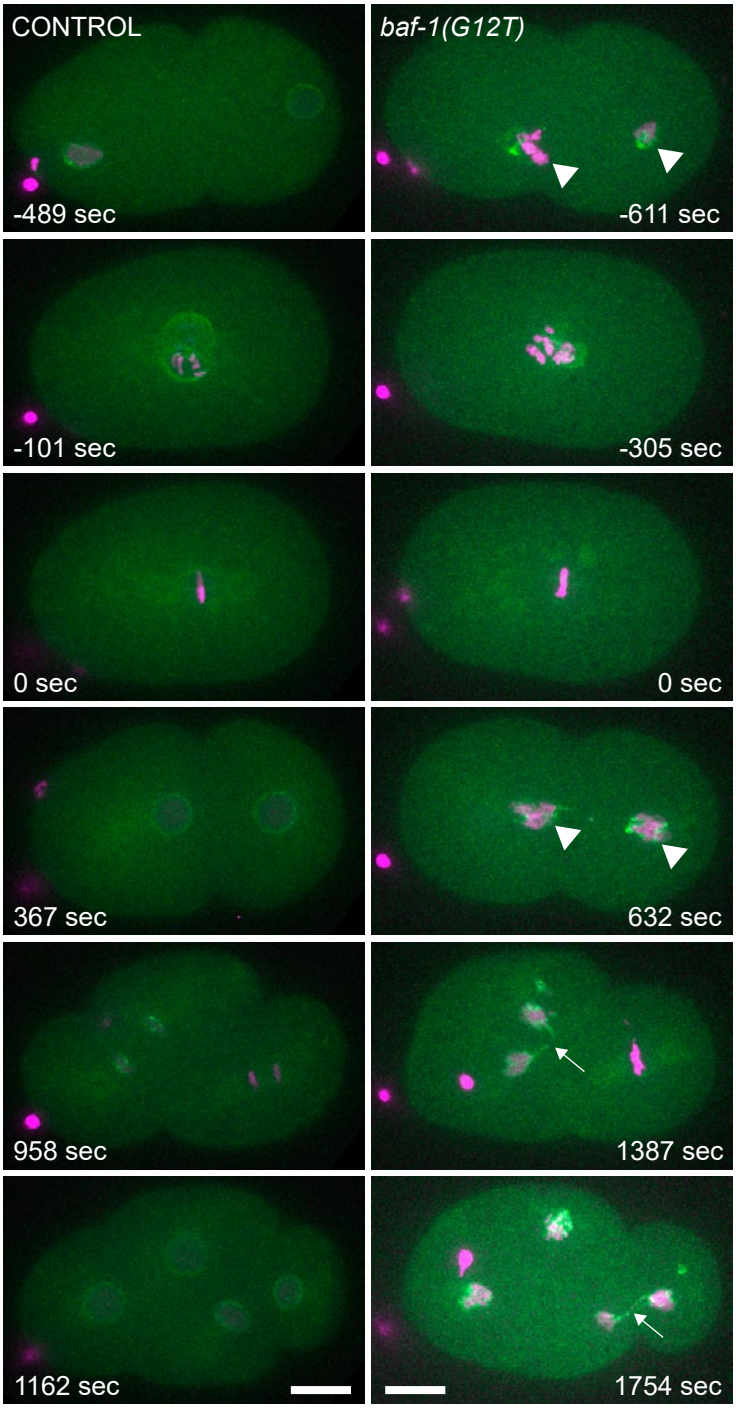

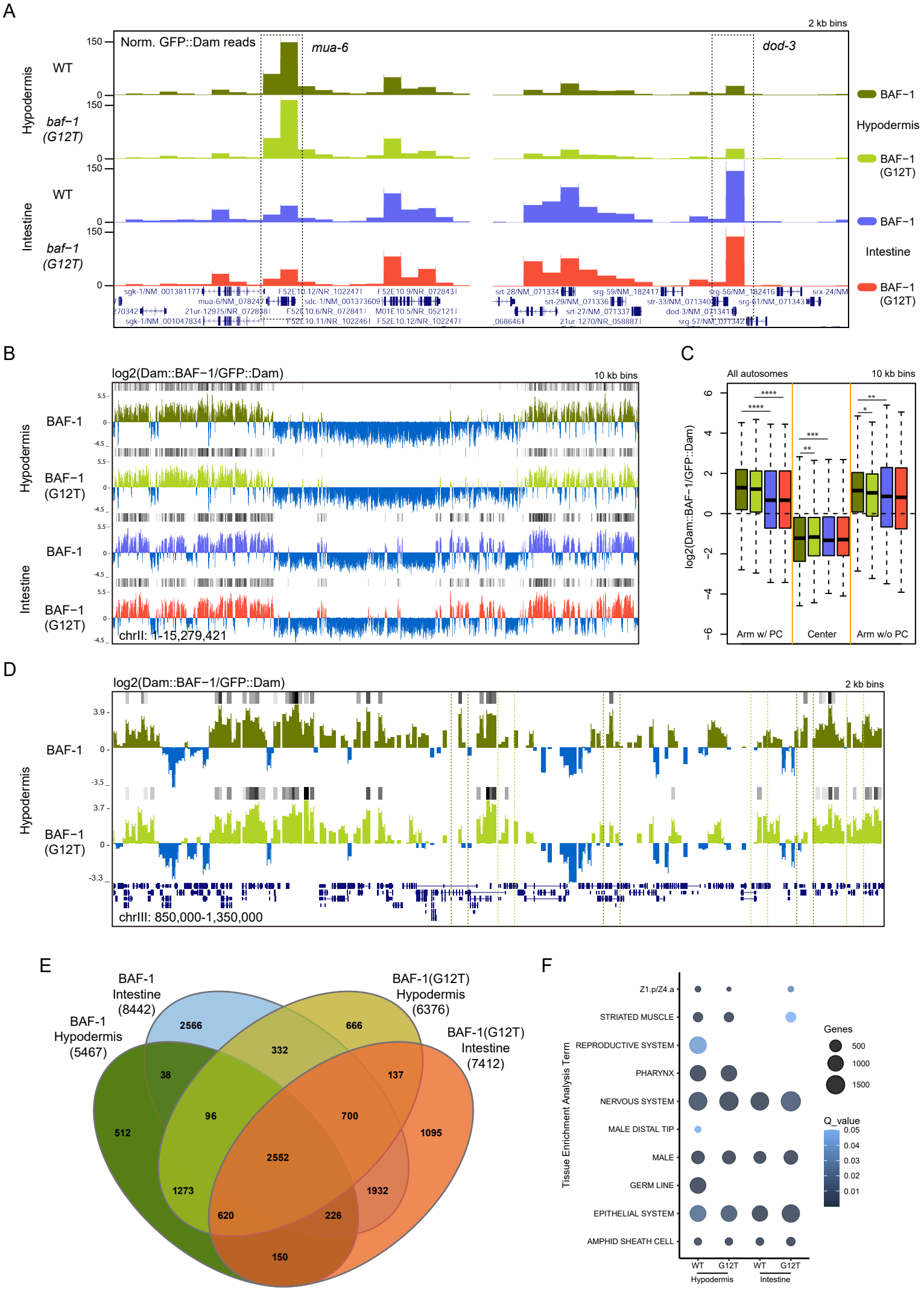
A
Norm. GFP::Dam reads
2 kb bins
mua-6
dod-3
Hypodermis
WT
baf−1 (G12T)
Intestine
WT
baf−1 (G12T)
BAF−1
Hypodermis
BAF−1 (G12T)
BAF−1
Intestine
BAF−1 (G12T)
B
log2(Dam::BAF−1/GFP::Dam)
10 kb bins
Hypodermis
BAF-1
BAF−1 (G12T)
Intestine
BAF-1
BAF−1 (G12T)
chrII: 1-15,279,421
C
All autosomes
10 kb bins
log2(Dam::BAF−1/GFP::Dam)
Arm w/ PC
Center
Arm w/o PC
D
log2(Dam::BAF−1/GFP::Dam)
2 kb bins
Hypodermis
BAF-1
BAF−1 (G12T)
chrIII: 850,000-1,350,000
E
BAF-1 Intestine (8442)
BAF-1(G12T) Hypodermis (6376)
BAF-1 Hypodermis (5467)
BAF-1(G12T) Intestine (7412)
2566
666
332
38
137
96
700
512
1095
2552
1273
1932
620
226
150
F
Tissue Enrichment Analysis Term
Z1.p/Z4.a
STRIATED MUSCLE
REPRODUCTIVE SYSTEM
PHARYNX
NERVOUS SYSTEM
MALE DISTAL TIP
MALE
GERM LINE
EPITHELIAL SYSTEM
AMPHID SHEATH CELL
WT
G12T
WT
G12T
Hypodermis
Intestine
Genes
500
1000
1500
Q_value
0.05
0.04
0.03
0.02
0.01

Figure 5

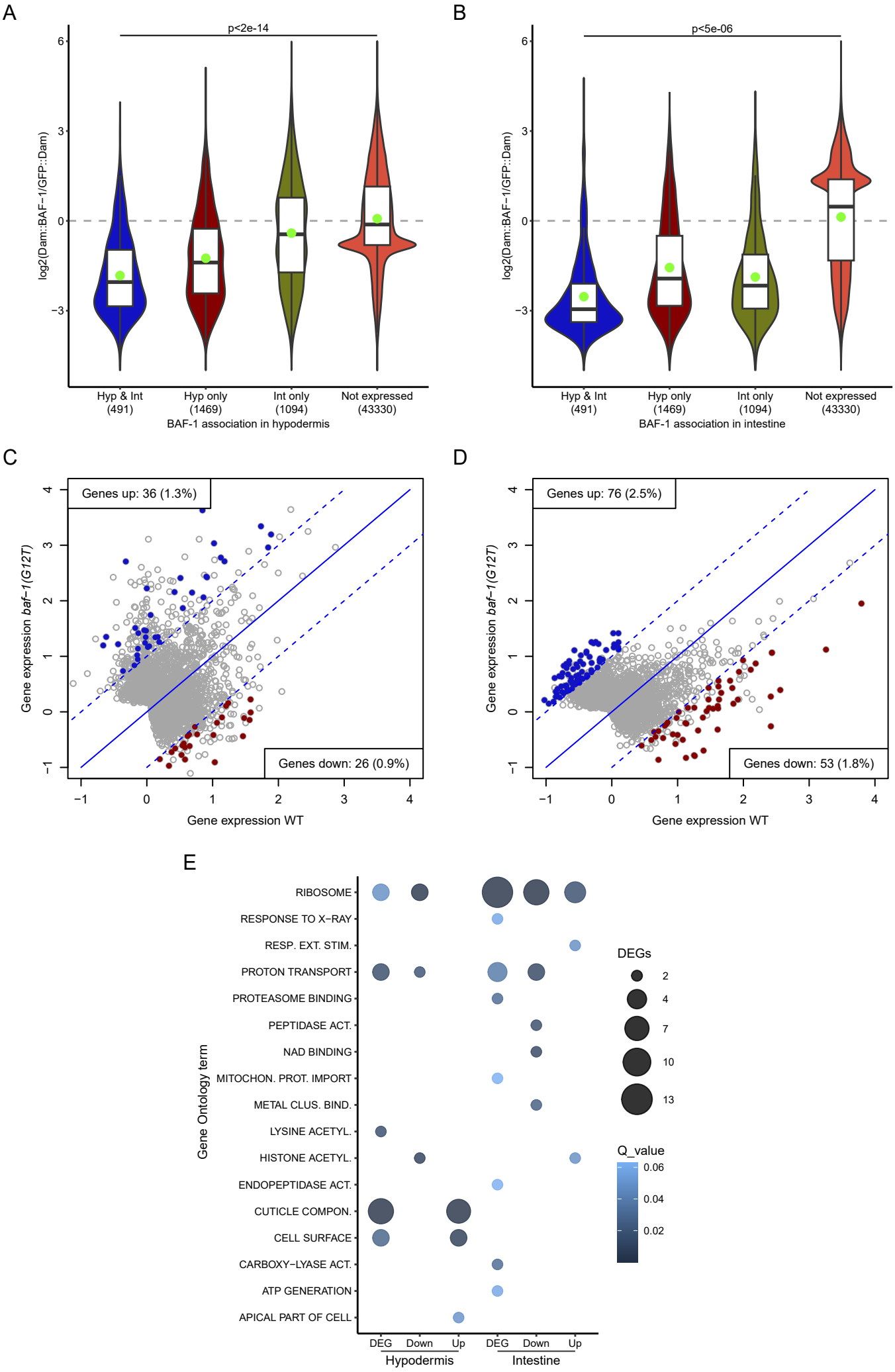
A
p<2e-14
log2(Dam::BAF−1/GFP::Dam)
Hyp & Int (491)
Hyp only (1469)
Int only (1094)
Not expressed (43330)
BAF-1 association in hypodermis
B
p<5e-06
log2(Dam::BAF−1/GFP::Dam)
Hyp & Int (491)
Hyp only (1469)
Int only (1094)
Not expressed (43330)
BAF-1 association in intestine
C
Genes up: 36 (1.3%)
Genes down: 26 (0.9%)
Gene expression baf−1(G12T)
Gene expression WT
D
Genes up: 76 (2.5%)
Genes down: 53 (1.8%)
Gene expression baf−1(G12T)
Gene expression WT
E
Gene Ontology term
RIBOSOME
RESPONSE TO X−RAY
RESP. EXT. STIM.
PROTON TRANSPORT
PROTEASOME BINDING
PEPTIDASE ACT.
NAD BINDING
MITOCHON. PROT. IMPORT
METAL CLUS. BIND.
LYSINE ACETYL.
HISTONE ACETYL.
ENDOPEPTIDASE ACT.
CUTICLE COMPON.
CELL SURFACE
CARBOXY−LYASE ACT.
ATP GENERATION
APICAL PART OF CELL
DEG Down Up DEG Down Up
Hypodermis
Intestine
DEGs
2
4
7
10
13
Q_value
0.06
0.04
0.02

Figure 6

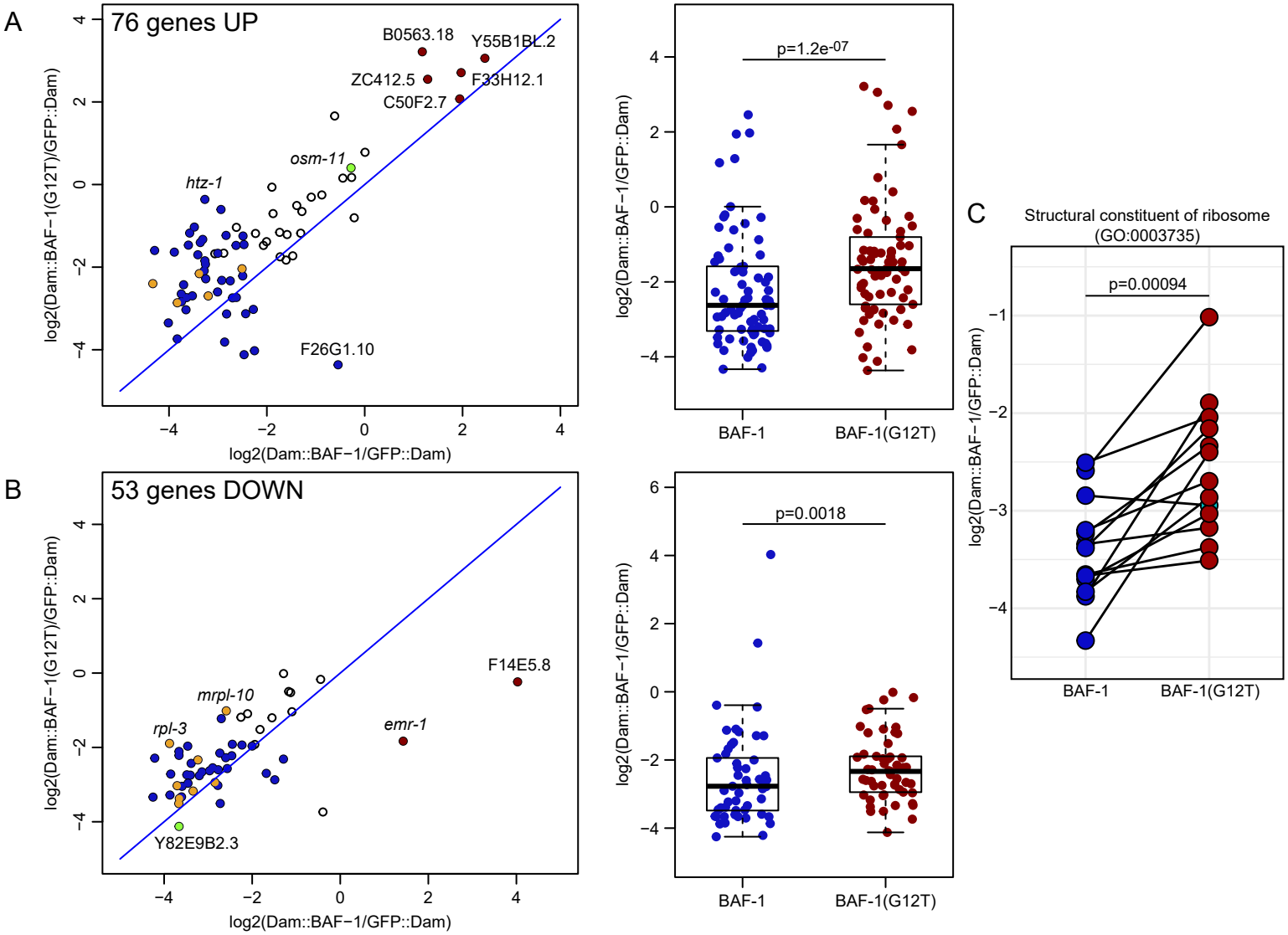
A
76 genes UP
B0563.18
Y55B1BL.2
ZC412.5
F33H12.1
C50F2.7
osm-11
htz-1
F26G1.10
log2(Dam::BAF−1(G12T)/GFP::Dam)
log2(Dam::BAF−1/GFP::Dam)
p=1.2e-07
BAF-1
BAF-1(G12T)
B
53 genes DOWN
F14E5.8
mrpl-10
rpl-3
emr-1
Y82E9B2.3
p=0.0018
C
Structural constituent of ribosome
(GO:0003735)
p=0.00094

Figure 7

A

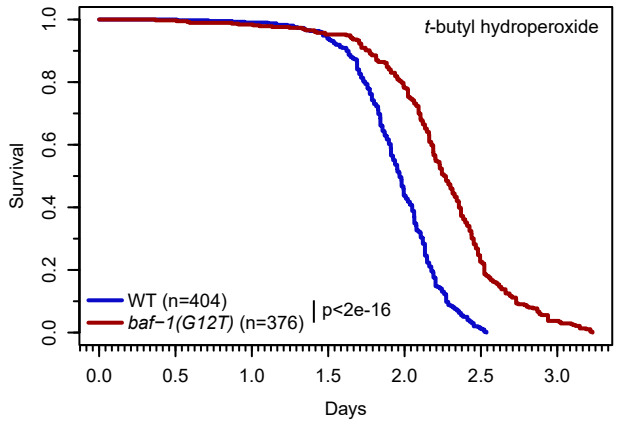
t-butyl hydroperoxide
Survival
1.0
0.8
0.6
0.4
0.2
0.0
WT (n=404)
baf−1(G12T) (n=376)
p<2e-16
0.0
0.5
1.0
1.5
2.0
2.5
3.0
Days

B

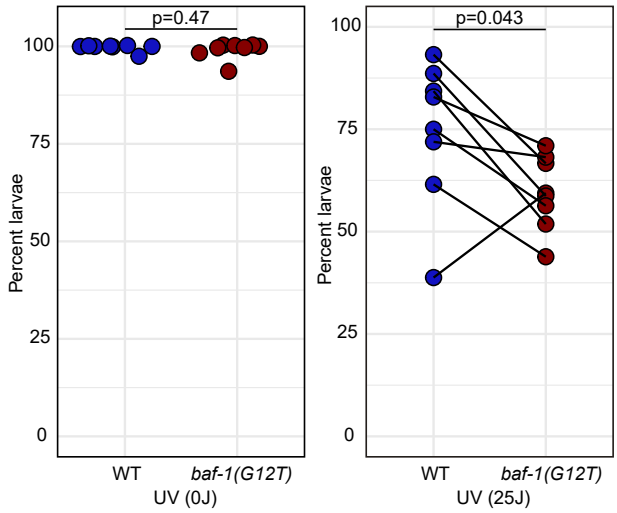
p=0.47
Percent larvae
100
75
50
25
0
WT
baf-1(G12T)
UV (0J)
p=0.043
Percent larvae
100
75
50
25
0
WT
baf-1(G12T)
UV (25J)

C

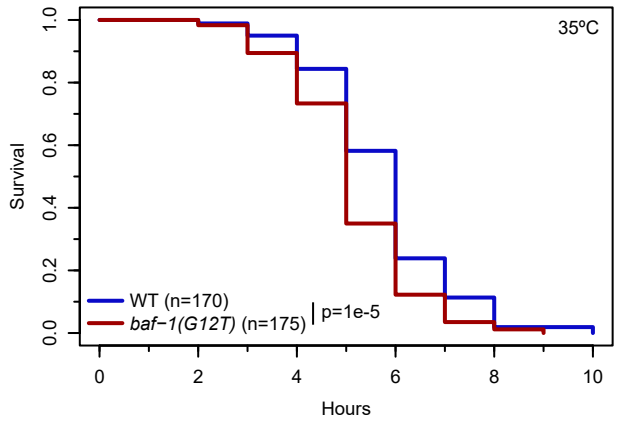
35ºC
Survival
1.0
0.8
0.6
0.4
0.2
0.0
WT (n=170)
baf−1(G12T) (n=175)
p=1e-5
0
2
4
6
8
10
Hours